

3

Differential Equation Methods for Scattering from Infinite Cylinders

Our investigation of numerical techniques for the analysis of infinite cylinders continues with formulations involving the two-dimensional scalar Helmholtz equations in the frequency domain. The integral equation approaches presented in Chapter 2 confined the unknown fields or currents to the surface or interior volume of the scatterer under consideration. In contrast, the computational domain associated with differential equation methods often includes an additional region of space outside the scatterer. To ensure that the scattered fields represent outward-propagating solutions, this region must be terminated with a radiation boundary condition. Exact and approximate radiation boundary conditions will be investigated. In addition, we consider two distinctly different ways of combining them with the Helmholtz equation to treat two-dimensional scattering.

Since different equivalent sources arise for dielectric, magnetic, and perfectly conducting materials, Chapter 2 presented separate integral equations for each type of scatterer. We adopt a more general approach in the present chapter and develop formulations capable of simultaneously treating scatterers containing any isotropic material. In fact, the procedure for treating highly heterogeneous materials with these techniques is identical to that used for homogeneous regions.

Because we strive for an introductory level of presentation, the discussion is limited to discretizations based on triangular-cell models of the cylinder cross section and piecewise-linear basis and testing functions. Extensions to other basis functions and more general cell shapes are deferred until Chapter 9. A sample computer program is described in Appendix D to illustrate the software implementation.

3.1 WEAK FORMS OF THE SCALAR HELMHOLTZ EQUATIONS

Consider a cylindrical scatterer characterized by a relative permittivity ϵ_r and permeability μ_r , that may vary with position (Figure 3.1). The electromagnetic fields produced in the

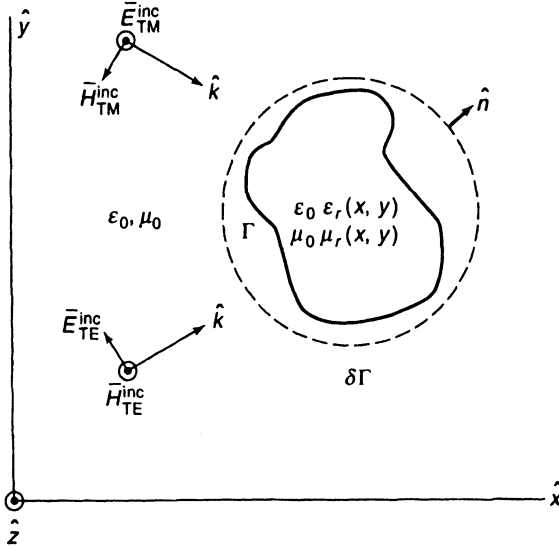


Figure 3.1 Inhomogeneity illuminated by an incident electromagnetic field. A mathematical boundary $\partial\Gamma$ encloses the scatterer.

vicinity of the cylinder by a TM illumination can be determined from the scalar Helmholtz equation

$$\nabla \cdot \left(\frac{1}{\mu_r} \nabla E_z \right) + k^2 \epsilon_r E_z = 0 \quad (3.1)$$

The analogous equation for the TE case involves the magnetic field and is

$$\nabla \cdot \left(\frac{1}{\epsilon_r} \nabla H_z \right) + k^2 \mu_r H_z = 0 \quad (3.2)$$

Equations (3.1) and (3.2) hold throughout a source-free region Γ containing the scatterer and must be augmented with boundary conditions on the surface $\partial\Gamma$ illustrated in Figure 3.1. The boundary conditions on $\partial\Gamma$ serve to couple the incident field into the equation and to ensure that the scattered field represents an outward-propagating solution. In principle, $\partial\Gamma$ may recede to infinity. In practice, $\partial\Gamma$ is located as close as possible to the scatterer surface in order to limit the number of required unknowns.

Equations (3.1) and (3.2) illustrate the “strong” form of the Helmholtz equations. In the strong form, the unknown appears within a second-order differential operator. To make these equations more amenable to numerical solution, they can be converted into their so-called “weak” form by multiplying both sides with a testing function $T(x, y)$ and performing an integration over Γ [1]. The vector identity

$$\nabla \cdot \{\bar{T}\bar{A}\} = T \nabla \cdot \bar{A} + \nabla T \cdot \bar{A} \quad (3.3)$$

and the divergence theorem

$$\iint_{\Gamma} \nabla \cdot \bar{A} dx dy = \int_{\partial\Gamma} \bar{A} \cdot \hat{n} dt \quad (3.4)$$

may be used to cast (3.1) and (3.2) into

$$\iint_{\Gamma} \left(\frac{1}{\mu_r} \nabla T \cdot \nabla E_z - k^2 \epsilon_r T E_z \right) dx dy = \int_{\partial\Gamma} \frac{1}{\mu_r} T \frac{\partial E_z}{\partial n} dt \quad (3.5)$$

$$\iint_{\Gamma} \left(\frac{1}{\epsilon_r} \nabla T \cdot \nabla H_z - k^2 \mu_r T H_z \right) dx dy = \int_{\partial\Gamma} \frac{1}{\epsilon_r} T \frac{\partial H_z}{\partial n} dt \quad (3.6)$$

Equations (3.5) and (3.6) are known as weak equations because the order of differentiation of the unknown fields is less than that of the original Helmholtz equations. By relaxing the strict differentiability requirements of the original equations, the weak equations permit the use of a wider variety of basis functions to represent the fields. In addition, medium discontinuities that would give rise to Dirac delta function terms in Equations (3.1) and (3.2) pose no such difficulty in Equations (3.5) and (3.6).

In deriving (3.5) and (3.6), we have tacitly assumed that the fields E_z and H_z are continuous functions. Later, when we introduce a subsectional basis representation for the fields, this assumption must be maintained in order to ensure the boundedness of ∇E_z and ∇H_z at cell interfaces. If the field representation is not assumed to be continuous, additional contour integrals arise between cells and can be included on the right-hand sides of (3.5) and (3.6). Our development will ignore these integrals and recapture them if needed (they will not be) via a Dirac delta dependence in ∇E_z and ∇H_z .

We will generally locate the surface $\partial\Gamma$ so that it completely encloses all inhomogeneities, leaving a buffer layer around the scatterer. Consequently, we will assume that $\mu_r = 1$ and $\epsilon_r = 1$ in the integrals over $\partial\Gamma$ appearing in (3.5) and (3.6) and omit the constitutive parameters from the boundary integrals in many of the examples to follow.

The introduction of a testing function to construct a weak equation may seem very different from the previous use of testing functions to approximately enforce integral equations (Chapter 2). In fact, the two procedures are completely analogous. In the formulation of Section 2.4, for instance, the integral equation was cast into a weak form by shifting a derivative onto the testing function. An apparent distinction arises because, in Chapter 2, testing functions were introduced as the final step of the discretization process. By employing testing functions as the first step of the process with differential equations, our attention is directed toward the boundary integrals over $\partial\Gamma$ in (3.5) and (3.6). These integrals provide a convenient way of incorporating boundary conditions and therefore play a prominent role in the formulation.

Boundary conditions may take several forms. The classical literature on boundary-value problems usually emphasizes conditions of the Dirichlet and Neumann variety. A Dirichlet type of boundary condition can be expressed as

$$E_z = f(t) \quad \text{on } \partial\Gamma \quad (3.7)$$

where f is a given function. If f is specified on the entire surface $\partial\Gamma$, Equation (3.1) or (3.5) uniquely describes E_z everywhere throughout Γ . A Neumann boundary condition prescribes the normal derivative of the unknown field on $\partial\Gamma$ and can be written

$$\frac{\partial E_z}{\partial n} = g(t) \quad \text{on } \partial\Gamma \quad (3.8)$$

where g is a given function. If g is specified on the entire boundary, Equation (3.1) or (3.5) again uniquely describes E_z throughout Γ . As a third possibility, a Dirichlet condition may be imposed on part of the boundary while a Neumann condition is imposed on the remaining part.

The given information in most electromagnetic scattering problems is limited to the target geometry and the incident field. The total field and its normal derivative are not initially known on a boundary surrounding the scatterer, and consequently Dirichlet and Neumann boundary conditions are not directly specified. Despite this, it is still possible

to pose the scattering problem in terms of indirect Dirichlet or Neumann conditions, and a formulation incorporating this idea will be described in Section 3.12.

Although the nature of scattering problems prevents the direct specification of Dirichlet or Neumann conditions on $\partial\Gamma$, boundary conditions can assume other forms. Two examples that often arise in electromagnetics are the impedance boundary conditions (Section 2.9) and the classical radiation boundary conditions (Section 1.3). These conditions have the form

$$\frac{\partial E_z}{\partial n} = h(t)E_z(t) \quad \text{on } \partial\Gamma \quad (3.9)$$

and relate the field and its normal derivative along $\partial\Gamma$ in such a way as to ensure unique solutions. If the incident field is known, an alternative statement of the scattering problem is to solve (3.5) or (3.6) to find the scattered field throughout Γ , subject to a radiation boundary condition (RBC) on $\partial\Gamma$ that forces the scattered field to propagate away from the region. In practice, this approach requires an RBC that can be applied close to the scatterer, in contrast to the Sommerfeld radiation condition from (1.36), which is only valid as $\rho \rightarrow \infty$. Several “near-field” radiation conditions will be developed in the following sections. These conditions are always more complicated than the simple Sommerfeld RBC, and for arbitrary boundary shapes they are only available in the form of integral equations. In addition, exact near-field RBCs are global conditions and couple the fields around the entire radiation boundary. In an attempt to facilitate an efficient numerical implementation, we will also consider one type of approximate RBC that is local in nature.

Generally, the most convenient way of incorporating boundary conditions such as (3.8) or (3.9) is by direct substitution into the surface integrals appearing on the right-hand sides of Equations (3.5) and (3.6). The resulting solution will satisfy the boundary condition in a weak sense, meaning that the degree of satisfaction is not exact for a finite number of basis functions. A Dirichlet condition, however, requires a substantially different implementation. The unknown function must be constructed from a basis that exactly satisfies the Dirichlet boundary condition (i.e., in the strong sense). The details of these two implementations will be discussed in the following section.

3.2 INCORPORATION OF PERFECTLY CONDUCTING BOUNDARIES

An obvious use of Dirichlet or Neumann boundary conditions is to incorporate materials within the scatterer geometry. Consider Figure 3.2, which depicts a p.e.c. region imbedded in a general scatterer. We redefine the interior volume Γ to exclude the conducting region and denote the surface of the conducting region $\partial\Gamma_c$ in order to distinguish it from the exterior surface $\partial\Gamma$. Equation (3.5) must be generalized to include the additional surface around the imbedded conductor and takes the modified form

$$\iint_{\Gamma} \left(\frac{1}{\mu_r} \nabla T \cdot \nabla E_z - k^2 \epsilon_r T E_z \right) dx dy = \int_{\partial\Gamma} T \frac{\partial E_z}{\partial n} dt + \int_{\partial\Gamma_c} \frac{1}{\mu_r} T \frac{\partial E_z}{\partial n} dt \quad (3.10)$$

where n is a local coordinate defined along the normal vector \hat{n} pointing out of Γ . The TM

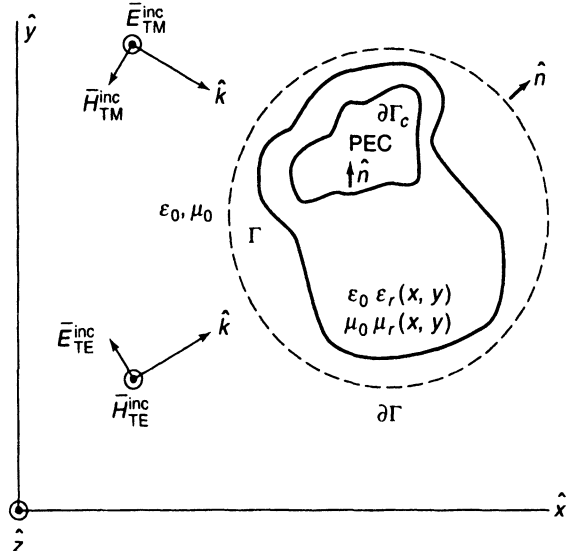


Figure 3.2 Cross section of the cylinder geometry showing the imbedded p.e.c. region whose surface is denoted $\partial\Gamma_c$.

fields must satisfy the Dirichlet boundary condition

$$E_z = 0 \quad \text{on } \partial\Gamma_c \quad (3.11)$$

The boundary condition in (3.11) can be enforced by building that behavior into the representation for E_z , or equivalently by zeroing the coefficient of any basis function that contributes to a nonzero E_z along $\partial\Gamma_c$. An alternative possibility is not to assign basis functions to $\partial\Gamma_c$ in the first place. In either case, there will be no unknowns associated with basis functions on $\partial\Gamma_c$, and the basis representation for E_z will exactly satisfy (3.11). Since there are no unknowns assigned to $\partial\Gamma_c$, there will be no need for testing functions along this boundary either. In practice, this implies that the integral over $\partial\Gamma_c$ in (3.10) does not contribute to the finite-element system and can be ignored. Thus, Equation (3.5) suffices, with the only modification necessary to incorporate (3.11) being to force the basis representation for E_z to vanish along the p.e.c. boundary.

For the TE polarization, the magnetic field at a perfectly conducting surface satisfies the Neumann boundary condition

$$\frac{\partial H_z}{\partial n} = 0 \quad \text{on } \partial\Gamma_c \quad (3.12)$$

Equation (3.6) can be modified to include the presence of the additional surface, yielding an equation for H_z of the form

$$\iint_{\Gamma} \left(\frac{1}{\epsilon_r} \nabla T \cdot \nabla H_z - k^2 \mu_r T H_z \right) dx dy = \int_{\partial\Gamma} T \frac{\partial H_z}{\partial n} dt + \int_{\partial\Gamma_c} \frac{1}{\epsilon_r} T \frac{\partial H_z}{\partial n} dt \quad (3.13)$$

To impose the Neumann boundary condition, Equation (3.12) is substituted into the boundary integral over $\partial\Gamma_c$ in (3.13). The integral vanishes, and (3.13) reverts back to the original form (3.6). In this case, values of H_z on $\partial\Gamma_c$ remain as unknowns to be determined, and consequently basis functions must be assigned to represent the nonzero field on this boundary. What has changed as a result of the Neumann condition? Although the weak equation remains unchanged, the scatterer geometry now excludes the region enclosed by $\partial\Gamma_c$ from

the problem domain. By not imposing any explicit condition on the fields adjacent to $\partial\Gamma_c$, the procedure automatically enforces (3.12) in a weak sense.

The Dirichlet boundary condition of Equation (3.11) is often denoted as an *essential* boundary condition, while the Neumann condition of Equation (3.12) is termed a *natural* boundary condition. The distinction between these is discussed by Strang and Fix [2]. The essential condition has to be explicitly built into the expansion functions in order to be satisfied by the solution, even in the limit of an infinite number of unknowns. In contrast, the natural condition will be satisfied in the limiting case, even if not satisfied by the individual expansion functions. For a finite number of basis functions, the natural boundary condition will only be satisfied in an approximate sense.

The Dirichlet and Neumann boundary conditions permit the incorporation of perfectly conducting material. To complete the formulation of the scattering problem, a radiation condition must be imposed along the outer boundary $\partial\Gamma$.

3.3 EXACT NEAR-ZONE RADIATION CONDITION ON A CIRCULAR BOUNDARY [3, 4]

If unconstrained by an appropriate boundary condition on $\partial\Gamma$, the scalar Helmholtz equation generally admits two solutions, one propagating away from the scatterer and one propagating toward the scatterer. To ensure a unique solution, some type of RBC must be imposed along $\partial\Gamma$. This RBC must ensure that the scattered field is propagating away from the cylinder and at the same time incorporate the incident field into the problem description.

Provided that the shape of $\partial\Gamma$ is constrained to be circular, an exact radiation boundary condition can be obtained from an exterior eigenfunction expansion. Assuming that we know the scattered electric field E_z^s on a circular boundary of radius $\rho = a$, the cylindrical eigenfunctions may be used to express the scattered fields exterior to the boundary as [5]

$$E_z^s(\rho, \phi) = \sum_{n=-\infty}^{\infty} e_n H_n^{(2)}(k\rho) e^{jn\phi} \quad \rho \geq a \quad (3.14)$$

where

$$e_n = \frac{1}{2\pi H_n^{(2)}(ka)} \int_0^{2\pi} E_z^s(a, \phi') e^{-jn\phi'} d\phi' \quad (3.15)$$

From this expansion, we construct

$$\frac{\partial E_z^s}{\partial \rho} = \sum_{n=-\infty}^{\infty} e_n k H_n^{(2)\prime}(k\rho) e^{jn\phi} \quad (3.16)$$

where the prime in (3.16) denotes differentiation with respect to the argument of the Hankel function. By substituting (3.15) into (3.16) and interchanging the order of summation and integration, we obtain

$$\left. \frac{\partial E_z^s}{\partial \rho} \right|_{\rho=a} = \int_0^{2\pi} E_z^s(a, \phi') \left[\frac{k}{2\pi} \sum_{n=-\infty}^{\infty} \frac{H_n^{(2)\prime}(ka)}{H_n^{(2)}(ka)} e^{jn(\phi-\phi')} \right] d\phi' \quad (3.17)$$

Although the form of Equation (3.17) is somewhat different from that of (3.9), it is an exact radiation boundary condition valid for finite ρ .

To facilitate a formulation in which the total electric field is the primary unknown, instead of the scattered field, Equation (3.17) can be combined with a similar expansion of the incident field. A plane-wave incident field can be expressed as [5]

$$E_z^{\text{inc}}(\rho, \phi) = \sum_{n=-\infty}^{\infty} e_n^{\text{inc}} J_n(k\rho) e^{jn\phi} \quad (3.18)$$

where

$$e_n^{\text{inc}} = \frac{1}{2\pi J_n(ka)} \int_0^{2\pi} E_z^{\text{inc}}(a, \phi') e^{-jn\phi'} d\phi' \quad (3.19)$$

By a similar procedure, we construct

$$\frac{\partial E_z^{\text{inc}}}{\partial \rho} = \sum_{n=-\infty}^{\infty} e_n^{\text{inc}} k J'_n(k\rho) e^{jn\phi} \quad (3.20)$$

and combine (3.19) and (3.20) to obtain

$$\left. \frac{\partial E_z^{\text{inc}}}{\partial \rho} \right|_{\rho=a} = \int_0^{2\pi} E_z^{\text{inc}}(a, \phi') \left(\frac{k}{2\pi} \sum_{n=-\infty}^{\infty} \frac{J'_n(ka)}{J_n(ka)} e^{jn(\phi-\phi')} \right) d\phi' \quad (3.21)$$

Equations (3.17) and (3.21) and the Wronskian relationship [5]

$$J'_n(ka) H_n^{(2)}(ka) - J_n(ka) H_n^{(2)\prime}(ka) = \frac{j^2}{\pi ka} \quad (3.22)$$

produce the alternative radiation boundary condition

$$\begin{aligned} \left. \frac{\partial E_z}{\partial \rho} \right|_{\rho=a} &= \int_0^{2\pi} E_z(a, \phi') \left(\frac{j}{\pi^2 a} \sum_{n=-\infty}^{\infty} \frac{1}{J_n(ka) H_n^{(2)}(ka)} e^{jn(\phi-\phi')} \right) d\phi' \\ &+ \int_0^{2\pi} E_z(a, \phi') \left(\frac{k}{2\pi} \sum_{n=-\infty}^{\infty} \frac{H_n^{(2)\prime}(ka)}{H_n^{(2)}(ka)} e^{jn(\phi-\phi')} \right) d\phi' \end{aligned} \quad (3.23)$$

This condition provides an exact relationship between the total and incident fields on a circular boundary of radius $\rho = a$. The same RBC describes the TE polarization, provided that E_z is replaced with H_z in Equation (3.23).

The second summation appearing in Equation (3.23) is divergent, since

$$\frac{H_n^{(2)\prime}(ka)}{H_n^{(2)}(ka)} \approx -\frac{|n|}{ka} \quad \text{as } |n| \rightarrow \infty \text{ with } ka \text{ fixed} \quad (3.24)$$

The divergent summation is a consequence of interchanging the integration and summation when constructing (3.17) and reflects the fact that the bracketed term in (3.17) behaves as a type of Green's function with a singularity at $\phi = \phi'$. Any computational difficulty, however, can be avoided by integrating term by term. The decay in the Fourier spectrum of $E_z(a, \phi)$ as $n \rightarrow \infty$ will ensure the convergence of the net result.

3.4 OUTWARD-LOOKING FORMULATION COMBINING THE SCALAR HELMHOLTZ EQUATION WITH THE EXACT RADIATION BOUNDARY CONDITION

The radiation boundary condition of Equation (3.23) can be substituted into Equation (3.5) to produce

$$\begin{aligned} & \iint_{\Gamma} \left(\frac{1}{\mu_r} \nabla T \cdot \nabla E_z - k^2 \epsilon_r T E_z \right) dx dy \\ & + \int_0^{2\pi} T(a, \phi) \int_0^{2\pi} E_z(a, \phi') G_2(\phi - \phi') d\phi' a d\phi \\ & = \int_0^{2\pi} T(a, \phi) \int_0^{2\pi} E_z^{\text{inc}}(a, \phi') G_1(\phi - \phi') d\phi' a d\phi \end{aligned} \quad (3.25)$$

where

$$G_1(\phi) = \frac{j}{\pi^2 a} \sum_{n=-\infty}^{\infty} \frac{1}{J_n(ka) H_n^{(2)}(ka)} e^{jn\phi} \quad (3.26)$$

and

$$G_2(\phi) = -\frac{k}{2\pi} \sum_{n=-\infty}^{\infty} \frac{H_n^{(2)\prime}(ka)}{H_n^{(2)}(ka)} e^{jn\phi} \quad (3.27)$$

Equation (3.25) provides a complete description of the TM scattering problem in terms of the interior E_z -field as the primary unknown to be determined. Because the equation is expressed explicitly in terms of interior field quantities (as if we stand inside the scatterer and look out), we denote this type of approach as an *outward-looking* formulation [6]. (This terminology will be clarified later in the chapter, when we introduce an alternative formulation we denote *inward looking*.)

Since the scatterer is inhomogeneous and arbitrary in shape, analytical solutions to (3.25) are usually not possible. Instead, we seek an approximate solution using basis and testing functions. Although the procedure to be followed is identical to the *method of moments* introduced in Chapter 2, it is popular usage to call it the *finite-element method* [1, 2, 7]. (Historically, the use of basis and testing functions to discretize integral equations of electromagnetics is most often named the “method of moments”; the same process applied to differential equations is usually known as the “weighted-residual” method or the “finite-element” method. Purists prefer to reserve the term finite-element method for variational methods, that is, explicitly minimizing a quadratic functional. However, for all aspects considered in this text the difference is only one of terminology.)

In order to discretize Equation (3.25) into matrix form, consider the division of the region Γ into triangular cells of constant permittivity and permeability, as depicted in Figure 3.3. We refer to the collection of cells as a *finite-element mesh* and introduce subsectional basis functions defined on the triangular-cell domain. The weak equation (3.25) involves the derivative ∇E_z , which will be unbounded unless E_z is continuous, and thus we exclude piecewise-constant basis functions from consideration. The simplest basis functions that provide a continuous representation for E_z are the linear “pyramid” functions introduced in Section 2.7, which are depicted in Figure 3.4. Each basis function has unity amplitude

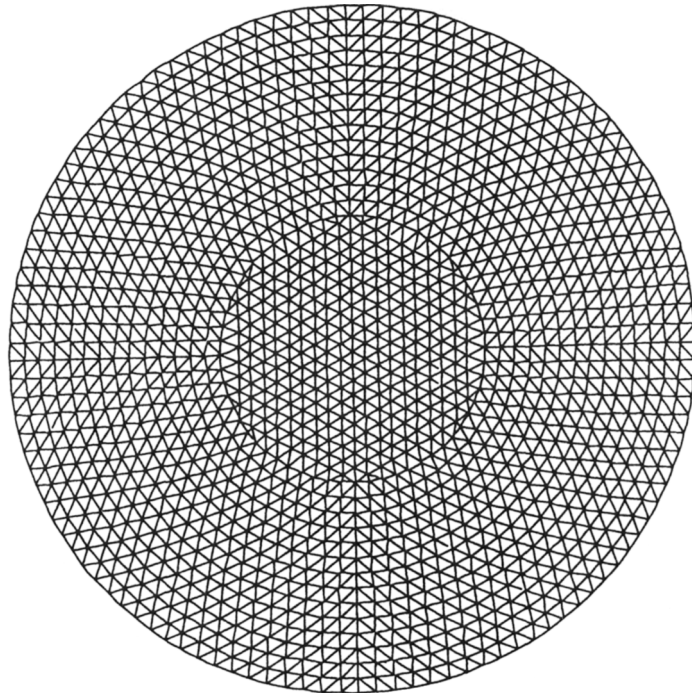


Figure 3.3 Triangular-cell mesh used to represent the cylinder cross section.

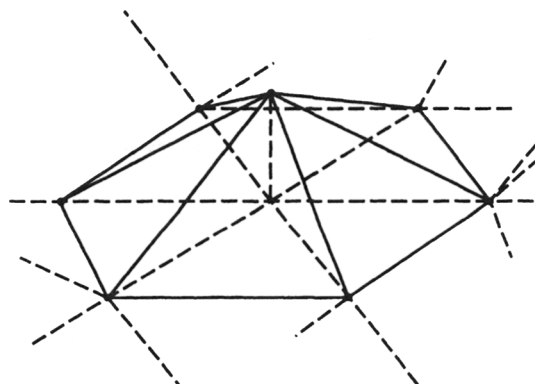


Figure 3.4 Linear pyramid basis function employed with the first-order finite-element representation.

at one node and vanishes at all other nodes in the mesh. Three basis functions overlap each triangular cell to provide a continuous piecewise-linear representation. If the mesh contains N nodes, the field representation can be expressed as

$$E_z(x, y) \cong \sum_{n=1}^N e_n B_n(x, y) \quad (3.28)$$

where $B_n(x, y)$ denotes a pyramid basis function centered at node n and e_n represents the interpolated value of E_z at that node. If (3.28) is substituted into Equation (3.25), N linearly independent equations can be generated using the same functions as testing functions:

$$T(x, y) = B_m(x, y) \quad m = 1, 2, \dots, N \quad (3.29)$$

The resulting matrix equation has the form

$$\mathbf{A}\mathbf{e} = \mathbf{b} \quad (3.30)$$

with entries given by

$$\begin{aligned} A_{mn} &= \iint_{\Gamma} \left(\frac{1}{\mu_r} \nabla B_m \cdot \nabla B_n - k^2 \varepsilon_r B_m B_n \right) dx dy \\ &\quad + \int_0^{2\pi} B_m(\phi) \int_0^{2\pi} B_n(\phi') G_2(\phi - \phi') d\phi' a d\phi \end{aligned} \quad (3.31)$$

and

$$b_m = \int_0^{2\pi} B_m(\phi) \int_0^{2\pi} E_z^{\text{inc}}(a, \phi') G_1(\phi - \phi') d\phi' a d\phi \quad (3.32)$$

Note that the first term in (3.31) represents an integration over the interior cross section Γ , while the second integral in (3.31) is a double integral over the boundary $\partial\Gamma$.

Consider the first integral over the interior region Γ appearing in Equation (3.31). Because each of the functions $\{B_n\}$ is nonzero only over a few cells of the mesh, this integral is zero except when basis and testing functions are centered at the same or immediately adjacent nodes. As a result of this “nearest-neighbor” or *local* interaction, many of the entries A_{mn} will be zero. We say that \mathbf{A} is a *sparse* matrix. The storage and computational requirements associated with a sparse-matrix equation can be significantly less than those of a full matrix, and several algorithms for the solution of sparse systems are discussed in Chapter 4.

As a general rule, the discretization of a differential operator usually produces a sparse matrix, in contrast to the full matrices produced by the integral operators considered in Chapter 2. Consequently, if compared with volume integral equation techniques (which require a computational domain Γ of similar overall size), differential equation formulations such as (3.25) are potentially more efficient and should enable the treatment of electrically larger regions.

The second term in (3.31) involves an integration over the radiation boundary condition imposed on $\partial\Gamma$. Unfortunately, this RBC is a *global* condition and couples information around the entire boundary. As a result, the part of the matrix with rows and columns associated with nodes on the boundary will be fully populated. For illustration, Figure 3.5 shows a hypothetical mesh and the resulting sparsity pattern in the \mathbf{A} matrix. The fill-in due to the global RBC is cause for concern, since it can significantly degrade the expected efficiency of the differential equation formulation. This difficulty has motivated the development of *local* boundary conditions that alleviate the fill-in problem, such as the Bayliss–Turkel boundary condition to be considered in Section 3.8.

We have now described the formulation in general terms but still need to develop a specific implementation for the entries of the matrix equation (3.30). Consider the boundary integral in (3.31),

$$I_{mn} = a \int_0^{2\pi} B_m(\phi) \int_0^{2\pi} B_n(\phi') G_2(\phi - \phi') d\phi' d\phi \quad (3.33)$$

Assuming that the triangular cells are small enough to closely approximate the curvature

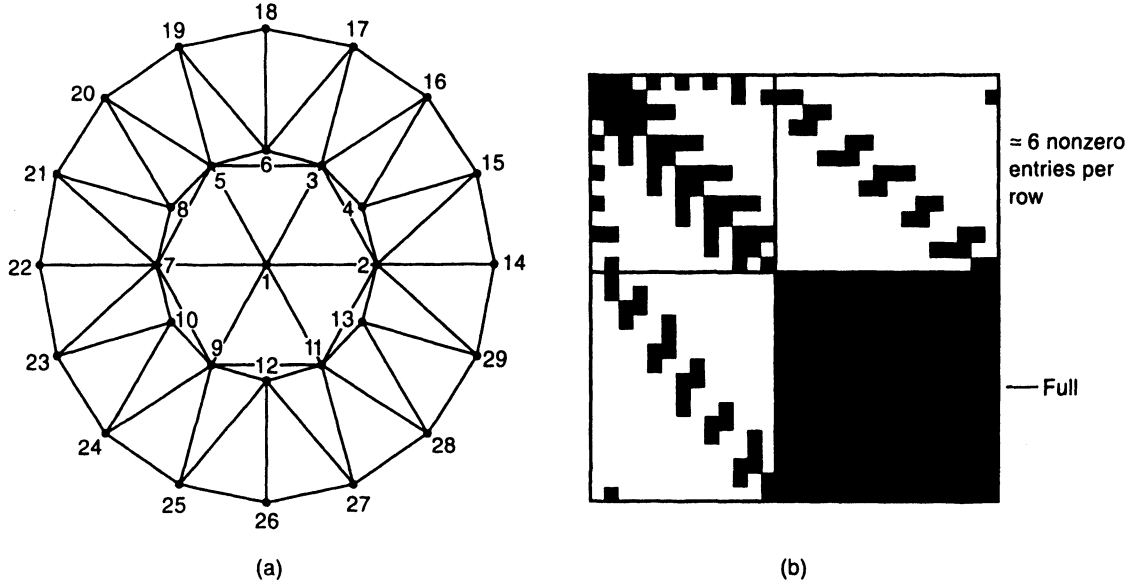


Figure 3.5 Triangular-cell mesh and the associated matrix sparsity pattern obtained with linear pyramid functions and the exact RBC.

of the circular boundary $\partial\Gamma$, B_m may be expressed along the boundary as

$$B_m(\phi) = \begin{cases} \frac{\phi - \phi_{m-1}}{\phi_m - \phi_{m-1}} & \phi_{m-1} < \phi < \phi_m \\ \frac{\phi_{m+1} - \phi}{\phi_{m+1} - \phi_m} & \phi_m < \phi < \phi_{m+1} \\ 0 & \text{otherwise} \end{cases} \quad (3.34)$$

where for convenience we denote the ϕ -coordinates of the three nodes associated with the m th basis function as ϕ_{m-1} , ϕ_m , and ϕ_{m+1} . After interchanging the order of integration and summation, we obtain

$$I_{mn} = -\frac{ka}{2\pi} \sum_{i=-\infty}^{\infty} \frac{H_i^{(2)\prime}(ka)}{H_i^{(2)}(ka)} \int_0^{2\pi} B_m(\phi) e^{ji\phi} d\phi \int_0^{2\pi} B_n(\phi') e^{-ji\phi'} d\phi' \quad (3.35)$$

A closed-form evaluation of the inner integrals is readily obtained in the form

$$\int_0^{2\pi} B_m(\phi) e^{ji\phi} d\phi = \frac{e^{ji\phi_m}}{i^2} \left(\frac{1 - e^{-ji(\phi_m - \phi_{m-1})}}{\phi_m - \phi_{m-1}} + \frac{1 - e^{ji(\phi_{m+1} - \phi_m)}}{\phi_{m+1} - \phi_m} \right) \quad (3.36)$$

Observe that the $O(i^{-2})$ decay in each integral is sufficient to ensure the convergence of the summation in (3.35), despite the $O(i)$ growth in the ratio of the Hankel functions.

The entries of the excitation vector from Equation (3.32) will be considered for a uniform plane-wave incident field of the form

$$E_z^{\text{inc}} = e^{-jk(x \cos \theta + y \sin \theta)} = \sum_{i=-\infty}^{\infty} j^{-i} J_i(k\rho) e^{ji(\phi - \theta)} \quad (3.37)$$

After interchanging the order of integration and summation, the required integral simplifies

to

$$b_m = \frac{j2}{\pi} \sum_{i=-\infty}^{\infty} \frac{1}{H_i^{(2)}(ka)} j^{-i} e^{-ji\theta} \int_0^{2\pi} B_m(\phi) e^{ji\phi} d\phi \quad (3.38)$$

which can also be evaluated using (3.36). Each entry of the excitation vector not associated with a testing function on the outer boundary is identically zero.

The remaining integrals involve the interior interaction of the basis and testing functions throughout Γ . These integrals consist of polynomial functions and can be evaluated exactly in closed form. We will consider their evaluation shortly (Section 3.7). First, however, let us explore a specific example to illustrate the solution process.

3.5 EXAMPLE: TM-WAVE SCATTERING FROM A DIELECTRIC CYLINDER

As a problem to illustrate the finite-element procedure, consider a TM plane wave incident on a circular dielectric cylinder and the task of determining the fields within the cylinder and the two-dimensional scattering cross section. The cylinder geometry will be represented by a triangular-cell mesh, and the interior E_z -field will be represented with piecewise-linear basis functions. For ease of implementation, let us assume that the circular outer boundary $\partial\Gamma$ is located one layer of cells away from the cylinder surface. Figure 3.5 shows a coarse finite-element mesh that could be used to describe the geometry, containing 40 cells and 29 nodes. The entire data structure describing this mesh would likely consist of (1) the number of cells, number of nodes, and number of nodes located on the outer boundary $\partial\Gamma$; (2) a list of the x , y -coordinates of each node; (3) a list giving the indices of the three nodes associated with each of the 40 cells (the *connectivity* array); (4) a list of the constitutive parameters of each cell; and (5) a list giving the indices of all the nodes located along the outer boundary, perhaps in order of increasing cylindrical angle ϕ (or possibly a boundary connectivity array listing the two node indices associated with each boundary edge).

To construct the global finite-element system $\mathbf{A}\mathbf{e} = \mathbf{b}$, the matrix entries given in Equations (3.31) and (3.32) must be computed for all possible combinations of basis and testing functions. The boundary integrals have been evaluated in (3.35)–(3.38), and the indices of the boundary basis and testing functions can be determined using the boundary pointer array in the mesh data structure. In other words, if nodes m and n are both located on the radiation boundary, there will be a contribution from I_{mn} in (3.35) to entry A_{mn} , and a contribution to both b_m and b_n from (3.38). The angles defining the limits of these integrals can be determined from the x , y -coordinates tabulated in the mesh data structure. If either index m or n refers to an interior node, there will be no boundary contribution to that location in \mathbf{A} .

The remaining integral in (3.31) represents the interaction of the basis and testing functions throughout the interior Γ . The interior interaction embodied in a single entry of \mathbf{A} involves integrals over a variable number of triangular cells. For example, there are six cells surrounding node 1 in Figure 3.5, implying that the evaluation of entry A_{11} involves integrals over six different cells. However, the data structure describing the finite-element mesh does not provide a direct way of determining the indices of these six cells, or even an

easy way of determining that there are precisely six cells adjacent to node 1. The situation may even be worse for an entry such as A_{13} , since the program would have to determine if any cells are shared by the basis and testing functions at nodes 1 and 3 (two are) and which cell indices were involved. In general, to evaluate entry A_{mn} directly, the computer program would require access to the number of cells touching each node, the indices of these cells, and a list of the other nodes associated with each of these cells. Fortunately, there is an easier (although conceptually indirect) way of computing the entries of \mathbf{A} .

To minimize the amount of data needed to define the mesh structure, the entries of \mathbf{A} can be evaluated on a cell-by-cell basis instead of a node-by-node approach. For any cell in the mesh, the connectivity array in the mesh data structure can be used to identify the x , y -coordinates of the vertices of that cell, after which the nine integrals arising from the possible combinations of the three testing functions and the three basis functions can be evaluated. Once these integrals have been evaluated, they make up the 3×3 *element matrix* associated with that cell. The nine numbers in the element matrix can be added to the appropriate locations in \mathbf{A} , using the connectivity array to identify the global indices (i.e., the row and column locations in \mathbf{A}) of the three nodes. The cell-by-cell approach permits the matrix entries to be constructed without knowing how many cells are shared by two adjacent basis functions. In addition, the element matrix entries depend only on the cell coordinates and can be conveniently evaluated in a standard subroutine.

For illustration, a hypothetical portion of the connectivity array associated with the mesh of Figure 3.5 is displayed in Table 3.1. Observe from the table that cell 3 is located between nodes 7, 1, and 5. The integrals over cell 3 can be evaluated and stored temporarily in the 3×3 element matrix. (The closed-form evaluation of the necessary integrals will be discussed in Section 3.7.) Element matrix entry E_{11} actually represents the portion of A_{77} that involves an integration over cell 3, while entry E_{12} represents the portion of A_{71} , and so on. Once the nine entries of the element matrix are evaluated in a standard subroutine, the connectivity array can be used to transfer them into the appropriate location within \mathbf{A} .

TABLE 3.1 Portion of Connectivity Array Containing Relative Locations of Nodes and Cells in the Mesh Shown in Figure 3.5

Cell Number	Node 1	Node 2	Node 3
1	1	2	3
2	1	3	5
3	7	1	5
:	:	:	:
25	7	8	21
26	7	21	22
27	7	22	23
28	7	10	23

Note: Each row “points” to the indices of the three nodes associated with that cell.

As the matrix entries are evaluated, the sparse global matrix \mathbf{A} is constructed and stored in some manner designed to minimize memory requirements and yet remain compatible with

a suitable matrix solution algorithm. We defer a discussion of sparse matrix organization and solution to Chapter 4.

After $\mathbf{Ae} = \mathbf{b}$ has been solved to produce the coefficients of E_z at each node of the mesh, secondary calculations such as the bistatic scattering cross section $\sigma(\phi)$ can be performed. There are several different ways of obtaining the scattering cross section, including the direct integration over equivalent electric and magnetic sources distributed throughout the penetrable scatterer or located on its surface, as discussed in Section 1.11 and Chapter 2. However, since the boundary $\partial\Gamma$ is circular in this case, a simpler alternative is an eigenfunction expansion of the exterior fields. In the TM case, the total fields external to $\partial\Gamma$ have the form [5]

$$E_z(\rho, \phi) = \sum_{n=-\infty}^{\infty} j^{-n} [J_n(k\rho)e^{-jn\theta} + \alpha_n H_n^{(2)}(k\rho)] e^{jn\phi} \quad (3.39)$$

where θ defines the polar angle into which the incident plane wave propagates. The coefficients can be found from the decomposition of the boundary E_z -field according to

$$\alpha_n = \frac{j^n (1/2\pi) \int_0^{2\pi} E_z(a, \phi) e^{-jn\phi} d\phi - J_n(ka) e^{-jn\theta}}{H_n^{(2)}(ka)} \quad (3.40)$$

where a is the radius of the outer boundary. The scattering cross section is given by

$$\sigma_{TM}(\phi) = \frac{4}{k} \left| \sum_{n=-\infty}^{\infty} \alpha_n e^{jn\phi} \right|^2 \quad (3.41)$$

Similar expressions involving the H_z -field can be used to find the scattering cross section for the TE polarization. It should be noted that the eigenfunction expansion procedure seems more sensitive to error in the field values than the direct volume integration method of computing σ discussed in Section 1.11 [8]. Although apparently more accurate, the direct integration method is more difficult to implement because it requires additional pointer arrays to describe the cell-to-edge connectivity and involves volumetric integrations over Γ rather than integrals along the boundary $\partial\Gamma$.

To illustrate the accuracy and convergence of the numerical results produced by the formulation, consider a circular dielectric cylinder with one wavelength circumference ($ka = 1$) and relative permittivity $\epsilon_r = 3$. Figures 3.5 and 3.6 illustrate typical triangular-cell models containing 29 and 51 nodes, respectively. A plot of the total E_z -field produced along a cut through the center of the dielectric cylinder by a TM wave incident in the \hat{x} direction is shown in Figure 3.7. The numerical results obtained with linear basis and testing functions exhibit good agreement with the exact solution and improve as the cell density is increased. These numerical results were obtained with a 51-node model having $\partial\Gamma$ located at $\rho = 0.22\lambda_0$ and 83- and 117-node models having the outer boundary located at $\rho = 0.20\lambda_0$ (λ_0 is the free-space wavelength). Numerical values for the magnitude and phase of the total E_z -field at the cylinder center are provided in Table 3.2 for these results and results from a fourth cylinder model employing 29 nodes with the RBC imposed at $\rho = 0.25\lambda_0$ and a fifth model having 255 nodes with $\partial\Gamma$ located at $\rho = 0.20\lambda_0$. For each model, Table 3.2 shows the density of nodes within the scatterer and the largest cell edge.

Table 3.2 also presents the percentage error associated with each solution. A study of this error suggests that it decreases roughly in proportion to $O(\Delta^2)$ as $\Delta \rightarrow 0$, where Δ is

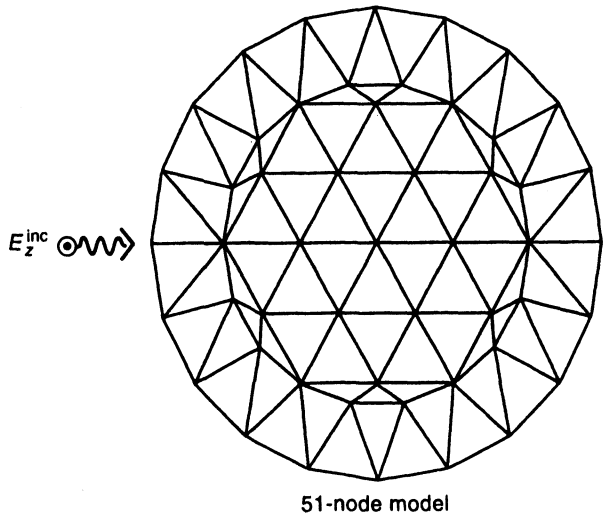


Figure 3.6 A 51-node triangular-cell model.

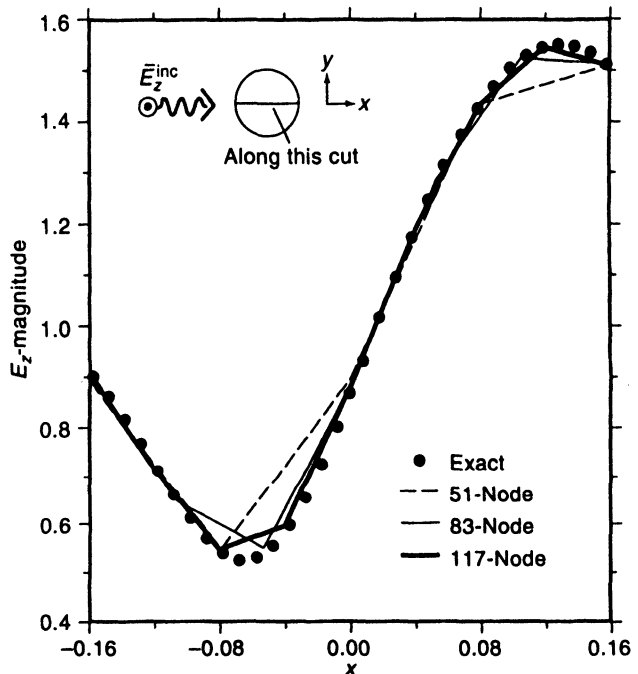


Figure 3.7 The TM electric field within a homogeneous dielectric cylinder with circumference $1.0\lambda_0$ and relative permittivity $\epsilon_r = 3$. The exact solution is compared with several first-order finite-element results.

the largest edge in the finite-element mesh. This behavior is consistent with the theoretical interpolation error associated with piecewise-linear basis functions (Chapter 5).

Table 3.3 presents scattering cross section data for the cylinder having $ka = 1$ and $\epsilon_r = 3$, obtained from a decomposition of the boundary fields according to (3.39)–(3.41). The numerical data appear to be converging toward the exact solution as the cell density is increased. These models have a density of unknowns in excess of $100 \text{ nodes}/\lambda_d^2$ and produce numerical results for scattering cross section exhibiting an error of less than 1 dB.

TABLE 3.2 Numerical Values of E_z -Field Produced at Center of Circular Dielectric Cylinder with $\epsilon_r = 3$ and $ka = 1$

Model	Average Node Density (nodes/ λ_d^2)	Longest Edge in Mesh (λ_0)	Magnitude of E_z	Phase of E_z (deg)	Percent Error
29-Node	54	0.163	0.992	-50.63	14.9
51-Node	130	0.093	0.915	-55.20	4.1
83-Node	230	0.057	0.903	-56.44	1.8
117-Node	356	0.054	0.898	-56.76	1.1
255-Node	683	0.032	0.895	-57.09	0.5
Exact	—	—	0.892	-57.36	—

Note: Results from five triangular-cell models are compared with the exact solution.

TABLE 3.3 Two-Dimensional Bistatic Scattering Cross Section^a σ_{TM} for Circular Dielectric Cylinder with $ka = 1$ and $\epsilon_r = 3$

ϕ (deg)	51-Node	83-Node	117-Node	255-Node	Exact
0	-0.24	0.09	0.17	0.24	0.289
30	-0.65	-0.37	-0.30	-0.23	-0.192
60	-1.87	-1.69	-1.64	-1.60	-1.567
90	-3.71	-3.62	-3.60	-3.57	-3.550
120	-5.56	-5.51	-5.51	-5.49	-5.469
150	-6.68	-6.62	-6.60	-6.58	-6.554
180	-6.97	-6.90	-6.88	-6.85	-6.819

^a In decibels free-space wavelength.

Note: Numerical results obtained using four cylinder models are compared with the exact solution.

3.6 SCATTERING FROM CYLINDERS CONTAINING CONDUCTORS

To illustrate the treatment of conducting material imbedded in the region Γ , we consider the problem of a circular conducting cylinder of radius $0.25\lambda_0$ coated with a homogeneous layer of dielectric having $\epsilon_r = 4$ and outer radius $0.30\lambda_0$. Two triangular-cell models will be employed having 22 and 44 nodes on the conductor and a total of 106 and 200 nodes, respectively. Both models contain three layers of cells around the conductor, two in the dielectric coating and a third outside the coating and terminating at $\rho = 0.33\lambda_0$.

For the TM polarization, the matrix A can be constructed as outlined in the preceding section, except that special treatment is required to account for the p.e.c. boundary. As discussed in Section 3.2, there is no need to assign unknowns for E_z along the conductor boundary $\partial\Gamma_c$, and there will be no basis or testing functions (and no rows or columns in the system matrix) associated with nodes located on $\partial\Gamma_c$. Consequently, the order of the global system will be smaller than the number of nodes in the mesh. (The matrix

orders associated with the two models of the coated cylinder discussed above are 84 and 156, respectively.) Since the nodes do not exhibit a one-to-one relationship with rows and columns of the system matrix, a more complex numbering scheme must be used to associate node indices with row and column indices. Perhaps the simplest scheme is to order the node indices so that any nodes on p.e.c. boundaries appear at the end of the list, leaving a one-to-one correspondence between the remaining nodes and the row and column indices. For each triangular cell bordering $\partial\Gamma_c$, the nine-element matrix entries are again obtained in the usual manner. However, only entries associated with interior nodes are transferred to the global system. In order to facilitate the identification and exclusion of the appropriate element matrix entries, an additional pointer array is required to identify nodes on $\partial\Gamma_c$.

A more general approach for the TM case would instead employ a pointer assigning a row and column index to each node at which an unknown is located and simultaneously identifying nodes on conducting boundaries. A third approach is to introduce “dummy” unknowns associated with p.e.c. boundary nodes in order to preserve the one-to-one relationship between the node indices and the row and column indices at the price of a slightly larger matrix order. Since the coefficients are known a priori, the rows associated with boundary nodes must be replaced with rows from an identity matrix, and the associated entries of the right-hand side are set to zero in order to force those coefficients to vanish after matrix solution. Since these rows are treated specially, the additional pointer is still required to identify boundary nodes. Thus, there does not appear to be a computational advantage to the use of dummy unknowns.

Table 3.4 presents the TM scattering cross section σ_{TM} for the coated cylinder geometry. Similar data for the TE polarization (σ_{TE}) is presented in Table 3.5. The TE formulation is obtained by exchanging ϵ_r and μ_r and replacing E_z with H_z in Equation (3.25). For the TE polarization, the H_z -field values on $\partial\Gamma_c$ remain unknowns to be determined, and all nine entries of each element matrix contribute to \mathbf{A} . The order of the system matrix is equal to the number of nodes in the mesh, and no additional pointers are needed to identify p.e.c. boundary nodes since they are not treated differently from the interior nodes. In essence, by placing a “hole” somewhere in the mesh and imposing no special boundary condition around it, the TE formulation will automatically treat that region as a perfect conductor.

TABLE 3.4 Bistatic Scattering Cross Section^a σ_{TM} for Circular Conducting Cylinder with Radius $0.25\lambda_0$ Coated with Dielectric Layer Having $\epsilon_r = 4$ and Outer Radius $0.3\lambda_0$

ϕ (deg)	106-Node	200-Node	Exact
0	5.45	5.41	5.372
30	3.79	3.77	3.748
60	0.05	0.05	0.043
90	-1.15	-1.19	-1.209
120	-0.73	-0.74	-0.749
150	-0.64	-0.64	-0.634
180	-0.63	-0.63	-0.627

^a In decibels free-space wavelength.

Note: Numerical results obtained using two cylinder models are compared with the exact solution.

TABLE 3.5 Bistatic Scattering Cross Section^a σ_{TE} for Circular Conducting Cylinder with Radius $0.25\lambda_0$ Coated with Dielectric Layer Having $\epsilon_r = 4$ and Outer Radius $0.3\lambda_0$

ϕ (deg)	106-Node	200-Node	Exact
0	3.99	4.17	4.231
30	-0.11	0.00	0.034
60	-1.96	-1.91	-1.916
90	0.95	1.01	1.026
120	-1.83	-1.87	-1.864
150	-1.89	-1.86	-1.867
180	-0.19	-0.10	-0.107

^a In decibels free-space wavelength.

Note: Numerical results obtained using two cylinder models are compared with the exact solution.

For the TE polarization, the current density J_z on the imbedded conductor can be obtained directly from the coefficients for H_z at nodes bordering the conductor. Figure 3.8 compares the surface current magnitude obtained using the 106-node model with the exact solution. The agreement is excellent. For the TM polarization, the surface current J_z cannot be obtained directly from the coefficients for E_z but can be estimated by differentiating the E_z -field to obtain H_z . The process of differentiating reduces the accuracy of J_z compared with E_z . An alternative approach for calculating J_z is explored in Prob. P3.11.

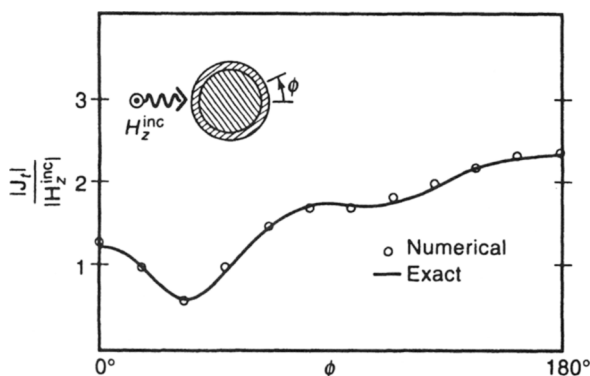


Figure 3.8 Comparison of the exact and numerical TE electric current density induced on the conducting surface of a circular p.e.c. cylinder imbedded within a circular dielectric shell by a uniform plane wave. The geometry is identical to that used in Tables 3.4 and 3.5.

3.7 EVALUATION OF VOLUMETRIC INTEGRALS FOR THE MATRIX ENTRIES [7]

The volume integral terms appearing in Equation (3.31) are common to scalar finite-element discretizations of the Laplace, Poisson, and Helmholtz equations and have been discussed in a variety of texts. In this section, we consider the evaluation of

$$A_{pq}^{(1)} = \iint_{\Gamma} \nabla B_p \cdot \nabla B_q \, dx \, dy \quad (3.42)$$

and

$$A_{pq}^{(2)} = \iint_{\Gamma} B_p B_q \, dx \, dy \quad (3.43)$$

where $\{B_q\}$ are linear pyramid functions (Figure 3.4) and the domain of integration is a single triangular cell. As discussed in preceding sections, the matrix A can be constructed indirectly by scanning through the mesh and evaluating the necessary integrals on a cell-by-cell basis. We will assume that the constitutive parameters ε_r and μ_r are constant within each cell of the mesh and therefore omit them from the integrals over a single cell.

Because the integrand consists of polynomials, the integrations can be evaluated in closed form. The evaluation over triangular cells is described in detail by Silvester and Ferrari [7]. It is convenient to carry out the analysis in terms of *simplex* coordinates $\{L_1, L_2, L_3\}$. These coordinates specify the position of a point within a triangle by giving the relative perpendicular distance measured from each side to the point, with the distance expressed as a fraction of the triangle altitude (Figure 3.9). Lines of constant L_i are parallel to side i of the triangle. (Each simplex coordinate is also the ratio of the area of the respective interior triangle formed by the point to the area of the entire triangle, hence the alternate name *local-area coordinates*.) The simplex coordinates are related to Cartesian coordinates by

$$x = L_1 x_1 + L_2 x_2 + L_3 x_3 \quad (3.44)$$

$$y = L_1 y_1 + L_2 y_2 + L_3 y_3 \quad (3.45)$$

where (x_i, y_i) are the coordinates of the i th vertex (see Figure 3.9). Since only two of the area coordinates can be independent, the additional condition

$$L_1 + L_2 + L_3 = 1 \quad (3.46)$$

is applied to yield

$$\begin{bmatrix} x \\ y \\ 1 \end{bmatrix} = \begin{bmatrix} x_1 & x_2 & x_3 \\ y_1 & y_2 & y_3 \\ 1 & 1 & 1 \end{bmatrix} \begin{bmatrix} L_1 \\ L_2 \\ L_3 \end{bmatrix} \quad (3.47)$$

Equation (3.47) can be inverted to produce

$$L_i = \frac{1}{2A} (a_i + b_i x + c_i y) \quad (3.48)$$

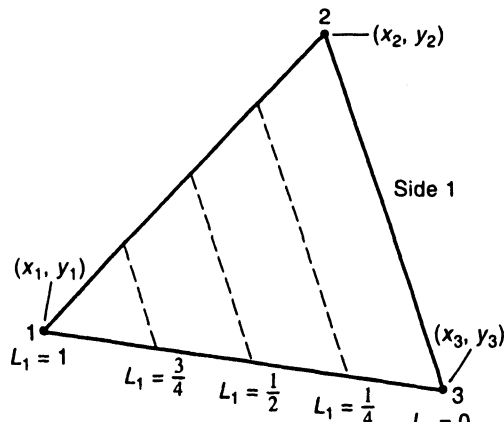


Figure 3.9 Local-area coordinate L_1 at different points throughout a triangular element.

where

$$a_i = x_{i+1}y_{i+2} - x_{i+2}y_{i+1} \quad (3.49)$$

$$b_i = y_{i+1} - y_{i-1} \quad (3.50)$$

$$c_i = x_{i-1} - x_{i+1} \quad (3.51)$$

and A represents the area of the triangle, that is,

$$A = \left| \frac{1}{2}(a_1 + a_2 + a_3) \right| = \left| \frac{1}{2}(b_{i+1}c_{i-1} - b_{i-1}c_{i+1}) \right| \quad (3.52)$$

The index i in Equations (3.49)–(3.52) assumes values 1, 2, and 3 cyclically, so that if $i = 3$, then $i + 1 = 1$.

Consider the evaluation of

$$A_{pq}^{(1)} = \iint_{\Gamma} \nabla B_p \cdot \nabla B_q \, dx \, dy \quad (3.53)$$

over one triangular cell Γ_i , where indices p and q range from 1 to 3 and represent the local index of the basis or testing function. (In other words, we seek to evaluate the 3×3 element matrix. These entries will subsequently be transferred into appropriate rows and columns of the global system using the connectivity matrix to map local indices to global indices.) Within the cell, linear pyramid basis functions are identical to the simplex coordinates themselves and can be expressed as

$$B_1(L_1, L_2, L_3) = L_1 \quad (3.54)$$

$$B_2(L_1, L_2, L_3) = L_2 \quad (3.55)$$

$$B_3(L_1, L_2, L_3) = L_3 \quad (3.56)$$

Since

$$\nabla L_i = \frac{1}{2A}(\hat{x}b_i + \hat{y}c_i) \quad (3.57)$$

the integrand of Equation (3.53) is constant and we immediately obtain

$$A_{pq}^{(1)} = \frac{b_p b_q + c_p c_q}{4A} \quad (3.58)$$

as an expression for the entries of the 3×3 element matrix.

The element matrix for the integral

$$A_{pq}^{(2)} = \iint_{\Gamma} B_p B_q \, dx \, dy \quad (3.59)$$

can be evaluated after transforming the integral from Cartesian coordinates to the simplex coordinates $\{L_1, L_2, L_3 = 1 - L_1 - L_2\}$ using the Jacobian relationship

$$dx \, dy = dL_1 \, dL_2 \frac{\partial(x, y)}{\partial(L_1, L_2)} = 2A \, dL_1 \, dL_2 \quad (3.60)$$

For the basis functions defined in (3.54)–(3.56), the integral

$$A_{pq}^{(2)} = 2A \iint_{\Gamma_i} B_p B_q \, dL_1 \, dL_2 \quad (3.61)$$

is a special case of the general formula [7]

$$I = \iint_{\Gamma_i} L_1^a L_2^b L_3^c \, dL_1 \, dL_2 = \frac{a!b!c!}{(a+b+c+2)!} \quad (3.62)$$

where a , b , and c represent integer powers. Therefore,

$$A_{pq}^{(2)} = \begin{cases} \frac{1}{6}A & p = q \\ \frac{1}{12}A & p \neq q \end{cases} \quad (3.63)$$

Thus, the entries of both element matrices are simple functions of the triangular-cell geometry.

In summary, the volumetric integrals within the matrix \mathbf{A} can be constructed on a cell-by-cell basis using element matrix entries from the simple closed-form expressions given in (3.58) and (3.63). These entries are subsequently multiplied with the constitutive parameters and added to appropriate locations within \mathbf{A} using the connectivity matrix to identify the global row and column indices. Appendix D describes a computer program incorporating this feature.

3.8 LOCAL RADIATION BOUNDARY CONDITIONS ON A CIRCULAR SURFACE: THE BAYLISS–TURKEL CONDITIONS [9]

The Helmholtz equation admits solutions for the scattered field that represent both outgoing and incoming waves. In classical electromagnetic analysis, a form of the Sommerfeld radiation condition

$$\lim_{\rho \rightarrow \infty} \frac{\partial E_z^s}{\partial \rho} = -jk E_z^s \quad (3.64)$$

is imposed on the boundary at infinity to suppress the inward-propagating part of the solution. Equation (3.64) is a *local* condition, since the derivative of the scattered field at a point on the boundary depends only on the field at that same point. Unfortunately, the Sommerfeld condition must be applied an infinite distance from the scatterer and is therefore not practical for near-field use. Although the exact RBC from Equation (3.17) is applicable for finite ρ , it is a *global* condition that couples field information around the entire boundary $\partial\Gamma$. In fact, any exact RBC valid for near-field use must be global. In an attempt to avoid the fill-in associated with exact global radiation conditions, several approximate RBCs have been developed that can be localized in a similar manner as the Sommerfeld condition. One family of near-field RBCs has been proposed by Bayliss and Turkel [9], and we review the derivation of those conditions in this section.

To derive a radiation or “absorbing” boundary condition that can be imposed in the near zone of a scatterer, note that an outward-propagating two-dimensional field may be expressed in the asymptotic form, valid for large ρ ,

$$E_z^s(\rho, \phi) \approx \frac{e^{-jkr}}{\sqrt{\rho}} \left(E_0(\phi) + \frac{E_1(\phi)}{\rho} + \frac{E_2(\phi)}{\rho^2} + \frac{E_3(\phi)}{\rho^3} + \dots \right) \quad (3.65)$$

or, in a more compact notation,

$$E_z^s \approx \frac{e^{-jkr}}{\sqrt{\rho}} \sum_{n=0}^{\infty} \frac{E_n(\phi)}{\rho^n} \quad (3.66)$$

As $\rho \rightarrow \infty$, Equation (3.65) satisfies the Sommerfeld condition. However, imposing the

Sommerfeld condition at finite ρ only forces the resulting solution to agree with the first term of (3.65), as can be demonstrated by writing

$$\frac{\partial E_z^s}{\partial \rho} \approx \frac{e^{-jk\rho}}{\sqrt{\rho}} \sum_{n=0}^{\infty} \left[-jk \frac{E_n(\phi)}{\rho^n} - \left(n + \frac{1}{2} \right) \frac{E_n(\phi)}{\rho^{n+1}} \right] \quad (3.67)$$

and combining Equations (3.66) and (3.67) to arrive at

$$\frac{\partial E_z^s}{\partial \rho} + jk E_z^s \approx \frac{e^{-jk\rho}}{\sqrt{\rho}} \sum_{n=0}^{\infty} \left[- \left(n + \frac{1}{2} \right) \frac{E_n(\phi)}{\rho^{n+1}} \right] \approx O(\rho^{-3/2}) \quad (3.68)$$

The Sommerfeld condition produces a spurious reflection of asymptotic order $O(\rho^{-3/2})$. In fact, since the residual produced by an outward-propagating wave is $O(\rho^{-3/2})$ while that produced by an inward-propagating wave is $O(\rho^{-1/2})$, the Sommerfeld radiation condition only provides an $O(\rho)$ degree of discrimination between incoming and outgoing waves. Although sufficient if applied at infinity, this RBC is not usually adequate for near-field use.

Bayliss and Turkel have derived a family of higher order radiation conditions that force the scattered field to agree with any number of terms from Equation (3.65) and provide a much greater degree of discrimination between inward-propagating and outward-propagating waves [9]. Their approach is based on the observation that the leading-order term in the residual on the right-hand side of (3.68) is

$$\frac{e^{-jk\rho}}{\sqrt{\rho}} \left(-\frac{1}{2} \frac{E_0(\phi)}{\rho} \right) \quad (3.69)$$

Since this quantity happens to equal the first term of (3.65) divided by -2ρ , we are motivated to inspect

$$\frac{\partial E_z^s}{\partial \rho} + jk E_z^s + \frac{E_z^s}{2\rho} \approx \frac{e^{-jk\rho}}{\sqrt{\rho}} \sum_{n=1}^{\infty} \left(-n \frac{E_n(\phi)}{\rho^{n+1}} \right) \approx O(\rho^{-5/2}) \quad (3.70)$$

In the asymptotic sense, an improved radiation condition can be obtained by equating the left-hand side of (3.70) with zero, to obtain the “first-order” RBC

$$\left(jk + \frac{\partial}{\partial \rho} + \frac{1}{2\rho} \right) E_z^s = 0 \quad (3.71)$$

Imposing (3.71) forces the solution to agree with the first two terms of the asymptotic expansion given in Equation (3.65), which should be an improvement over the Sommerfeld condition for finite ρ . Equation (3.71) provides an $O(\rho^2)$ degree of discrimination between the inward-propagating and outward-propagating waves.

The leading-order residual in (3.70) is

$$\frac{e^{-jk\rho}}{\sqrt{\rho}} \left(-\frac{E_1(\phi)}{\rho^2} \right) \quad (3.72)$$

Since (3.72) is not directly proportional to the leading-order term in the series for the scattered field, we are unable to continue combining simple multiples of the field to obtain

a reduction in the residual. However, observe that

$$\begin{aligned} & \frac{\partial}{\partial \rho} \left(\frac{\partial E_z^s}{\partial \rho} + jk E_z^s + \frac{E_z^s}{2\rho} \right) \\ & \approx \frac{e^{-jk\rho}}{\sqrt{\rho}} \sum_{n=1}^{\infty} \left(jkn \frac{E_n(\phi)}{\rho^{n+1}} + \frac{n}{2} \frac{E_n(\phi)}{\rho^{n+2}} + n(n+1) \frac{E_n(\phi)}{\rho^{n+2}} \right) \end{aligned} \quad (3.73)$$

The leading-order term of the residual series in (3.73) is

$$\frac{e^{-jk\rho}}{\sqrt{\rho}} \left(jk \frac{E_1(\phi)}{\rho^2} \right) \quad (3.74)$$

This immediately motivates the inspection of

$$\begin{aligned} \left(\frac{\partial}{\partial \rho} + jk \right) \left(\frac{\partial E_z^s}{\partial \rho} + jk E_z^s + \frac{E_z^s}{2\rho} \right) & \approx \frac{e^{-jk\rho}}{\sqrt{\rho}} \sum_{n=1}^{\infty} \left[n \left(n + \frac{3}{2} \right) \frac{E_n(\phi)}{\rho^{n+2}} \right] \\ & \approx O(\rho^{-7/2}) \end{aligned} \quad (3.75)$$

which has leading-order residual

$$\frac{e^{-jk\rho}}{\sqrt{\rho}} \left(\frac{5}{2} \frac{E_1(\phi)}{\rho^3} \right) \quad (3.76)$$

Continuing this procedure, we consider

$$\begin{aligned} \left(\frac{\partial}{\partial \rho} + jk + \frac{5}{2\rho} \right) \left(\frac{\partial E_z^s}{\partial \rho} + jk E_z^s + \frac{E_z^s}{2\rho} \right) & \approx \frac{e^{-jk\rho}}{\sqrt{\rho}} \sum_{n=1}^{\infty} \left(n(n-1) \frac{E_n(\phi)}{\rho^{n+2}} \right) \\ & \approx O(\rho^{-9/2}) \end{aligned} \quad (3.77)$$

From the size of the residual in (3.77), we conclude that imposing the “second-order” RBC

$$\left(jk + \frac{\partial}{\partial \rho} + \frac{5}{2\rho} \right) \left(jk + \frac{\partial}{\partial \rho} + \frac{1}{2\rho} \right) E_z^s = 0 \quad (3.78)$$

forces the numerical solution to agree with the first four terms of (3.65). Equation (3.78) provides an $O(\rho^4)$ degree of discrimination between the inward-propagating and outward-propagating waves and suppresses incoming waves down to $O(\rho^{-9/2})$.

The procedure outlined above can be continued, leading to the general N th order condition [9]

$$\prod_{n=1}^N \left(jk + \frac{\partial}{\partial \rho} + \frac{4n-3}{2\rho} \right) E_z^s = 0 \quad (3.79)$$

The N th-order Bayliss–Turkel RBC forces the solution to agree with the first $2N$ terms of the asymptotic expansion given in (3.65) and eliminates spurious reflections from the artificial boundary down to terms of order $O(\rho^{-2N-1/2})$.

We will be primarily interested in the second-order Bayliss–Turkel condition appearing in Equation (3.78). Using the scalar Helmholtz equation in cylindrical coordinates, this

condition can be rewritten in the form

$$\frac{\partial E_z^s}{\partial \rho} = \alpha(\rho) E_z^s + \beta(\rho) \frac{\partial^2 E_z^s}{\partial \phi^2} \quad (3.80)$$

where

$$\alpha(\rho) = \frac{-jk - 3/2\rho + j3/8k\rho^2}{1 - j/k\rho} \quad (3.81)$$

and

$$\beta(\rho) = \frac{-j/2k\rho^2}{1 - j/k\rho} \quad (3.82)$$

Because this boundary condition involves only second-order tangential derivatives, it is local in nature and does not couple the fields around the entire boundary. In fact, since it has an order of differentiation identical with that of the Helmholtz equation, it should lead to a comparable degree of sparsity after discretization. If used with linear pyramid expansion and testing functions, (3.80) will only couple information between adjacent cells around the periphery of Γ and introduce no additional fill-in beyond that already present due to internal interactions.

Except in the limit as $\rho \rightarrow \infty$, Equation (3.80) is approximate. The solution produced using the second-order RBC can be written in the vicinity of the boundary as

$$\begin{aligned} E_z^s &= \frac{e^{-jk\rho}}{\sqrt{\rho}} \left(E_0(\phi) + \frac{E_1(\phi)}{\rho} + \frac{E_2(\phi)}{\rho^2} + \frac{E_3(\phi)}{\rho^3} \right) \\ &\quad + \frac{e^{-jk\rho}}{\sqrt{\rho}} \left(\frac{A_4(\phi)}{\rho^4} + \dots \right) + \frac{e^{+jk\rho}}{\sqrt{\rho}} \left(\frac{B_4(\phi)}{\rho^4} + \dots \right) \end{aligned} \quad (3.83)$$

where $\{E_n\}$ are the “correct” outward-propagating terms produced by the Helmholtz equation and $\{A_n\}$ and $\{B_n\}$ denote terms that have been corrupted by the approximate RBC. Clearly, the Bayliss–Turkel condition will produce an accurate result only if the second and third summations in (3.83) are small compared with the first. This is easily accomplished in principle by making ρ large, but to minimize the number of unknowns, it is desirable to place $\partial\Gamma$ relatively close to the scatterer surface. As we shall demonstrate, accurate results can sometimes be obtained with boundaries almost circumscribing the scatterer. For these examples, the convergence rate of (3.65) appears to be very fast, so that terms such as A_4 and B_4 are negligible even for small ρ . However, in other situations the convergence rate of (3.65) may be quite slow. Canning has demonstrated the slow convergence of (3.65) for scattered waves emanating from locations other than the origin of the coordinate system [10]. In other words, it appears that the Bayliss–Turkel RBC will readily absorb a wave that is normally incident to the boundary but not a wave that approaches $\partial\Gamma$ at angles close to grazing. Consequently, if the geometry of interest happens to contain strong scattering centers located far from the origin, it may not be possible to locate $\partial\Gamma$ immediately adjacent to the scatterer. Numerical experimentation can provide useful feedback concerning the sensitivity of the results to boundary location.

An alternate approach for systematically studying the accuracy of the local RBC employs cylindrical harmonics [11]. An outward-propagating harmonic has the form

$$E_z^s(\rho, \phi) = E_0 H_n^{(2)}(k\rho) e^{jn\phi} \quad (3.84)$$

and will satisfy any exact radiation condition. For this n th harmonic, the second-order Bayliss–Turkel condition can be interpreted as an attempt to approximate the exact relationship

$$\frac{\partial E_z^s}{\partial \rho} = \frac{kH_n^{(2)\prime}(k\rho)}{H_n^{(2)}(k\rho)} E_z^s \quad (3.85)$$

with the approximate relationship

$$\frac{\partial E_z^s}{\partial \rho} \cong [\alpha(\rho) - n^2 \beta(\rho)] E_z^s \quad (3.86)$$

Equations (3.85) and (3.86) can be compared as a function of the radius of the outer boundary to determine the range of validity of the local RBC. Figure 3.10 presents a comparison for a boundary of radius $k\rho = 51$. Although the lower order harmonics satisfy the Bayliss–Turkel condition very well, the higher order harmonics do not. The agreement degenerates in the vicinity of $n = k\rho$, which for a given harmonic is the approximate region where the predominantly evanescent character ($k\rho < n$) of the Hankel functions changes to a propagating behavior ($k\rho > n$). The Bayliss–Turkel condition was based on the propagating form presented in Equation (3.65), and it is not surprising that the second-order RBC will fail for an evanescent field. In fact, the N th-order RBC would fail in an evanescent region even for arbitrarily large N . Consequently, for the Bayliss–Turkel RBC to work well, it appears that $\partial\Gamma$ must always be located beyond the evanescent region of the scatterer.

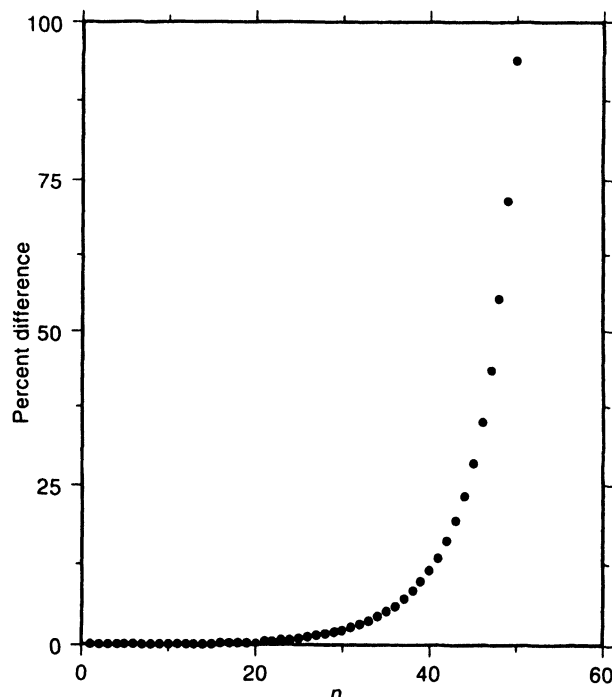


Figure 3.10 Comparison of Equations (3.85) and (3.86) as a function of the harmonic index n for $k\rho = 51$.

3.9 OUTWARD-LOOKING FORMULATION COMBINING THE SCALAR HELMHOLTZ EQUATION AND THE SECOND-ORDER BAYLISS–TURKEL RBC [12]

To illustrate the use of the local RBC, we return to the problem of TM-wave scattering from an inhomogeneous cylinder. Equation (3.80) can be substituted into the boundary integral of (3.5) and terms involving the incident field added in order to preserve the total field as the primary unknown. After integration by parts is employed to eliminate the second-order differential operator, the equation has the form

$$\begin{aligned} & \iint_{\Gamma} \left(\frac{1}{\mu_r} \nabla T \cdot \nabla E_z - k^2 \epsilon_r T E_z \right) dx dy - \int_{\partial\Gamma} \left(\alpha T E_z - \beta \frac{\partial T}{\partial \phi} \frac{\partial E_z}{\partial \phi} \right) \rho d\phi \\ &= \int_{\partial\Gamma} T \left(\frac{\partial E_z^{\text{inc}}}{\partial \rho} - \alpha E_z^{\text{inc}} - \beta \frac{\partial^2 E_z^{\text{inc}}}{\partial \phi^2} \right) \rho d\phi \end{aligned} \quad (3.87)$$

Equation (3.87) is an outward-looking formulation that can be used as an alternative to (3.25). Although the equation is approximate because of the second-order Bayliss–Turkel RBC, this formulation preserves the sparsity inherent in the differential equation and usually requires much less storage and computation than (3.25).

The finite-element discretization of Equation (3.87) proceeds in a manner similar to that carried out in Section 3.3 and produces a matrix equation

$$\mathbf{A}\mathbf{e} = \mathbf{b} \quad (3.88)$$

with entries given by

$$\begin{aligned} A_{mn} = & \iint_{\Gamma} \left(\frac{1}{\mu_r} \nabla B_m \cdot \nabla B_n - k^2 \epsilon_r B_m B_n \right) dx dy \\ & - \int_{\partial\Gamma} \left(\alpha B_m B_n - \beta \frac{\partial B_m}{\partial \phi} \frac{\partial B_n}{\partial \phi} \right) \rho d\phi \end{aligned} \quad (3.89)$$

and

$$b_m = \int_{\partial\Gamma} B_m \left(\frac{\partial E_z^{\text{inc}}}{\partial \rho} - \alpha E_z^{\text{inc}} - \beta \frac{\partial^2 E_z^{\text{inc}}}{\partial \phi^2} \right) \rho d\phi \quad (3.90)$$

where α and β are defined in Equations (3.81) and (3.82).

The evaluation of the volume integral terms in (3.89) for linear pyramid expansion and testing functions has already been discussed in Section 3.7. The additional calculations arising from boundary integrals

$$A_{pq}^{(3)} = \int_{\partial\Gamma} B_p B_q dt \quad (3.91)$$

and

$$A_{pq}^{(4)} = \int_{\partial\Gamma} \frac{\partial B_p}{\partial t} \frac{\partial B_q}{\partial t} dt \quad (3.92)$$

can be arranged in the form of 2×2 element matrices. For piecewise-linear basis functions spanning an interval of length w on the boundary, these integrals are easily evaluated to

produce

$$A_{pq}^{(3)} = \begin{cases} \frac{1}{3}w & p = q \\ \frac{1}{6}w & \text{otherwise} \end{cases} \quad (3.93)$$

and

$$A_{pq}^{(4)} = \begin{cases} \frac{1}{w} & p = q \\ -\frac{1}{w} & \text{otherwise} \end{cases} \quad (3.94)$$

Equation (3.90) can be determined for a plane-wave incident field of the form

$$E_z^{\text{inc}} = e^{-jk(x \cos \theta + y \sin \theta)} \quad (3.95)$$

by incorporating the intermediate result

$$\begin{aligned} \frac{\partial E_z^{\text{inc}}}{\partial \rho} - \alpha E_z^{\text{inc}} - \beta \frac{\partial^2 E_z^{\text{inc}}}{\partial \phi^2} \\ = -[\alpha + (1 + \beta \rho) j k \cos(\theta - \phi) - \beta k^2 \rho^2 \sin^2(\theta - \phi)] e^{-jk\rho \cos(\theta - \phi)} \end{aligned} \quad (3.96)$$

and evaluating the remaining integral.

If linear pyramid functions are employed for basis and testing, \mathbf{A} involves only nearest-neighbor interactions and has a high degree of sparsity. Figure 3.11 presents the sparsity pattern for the cylinder model previously illustrated in Figure 3.5, assuming linear basis and testing functions. The right-hand side of (3.90) is also sparse, as the nonzero entries are restricted to rows associated with nodes on the boundary.

To illustrate the validity of the formulation incorporating the second-order Bayliss–Turkel RBC, we return to the coated conducting cylinder previously considered in Section

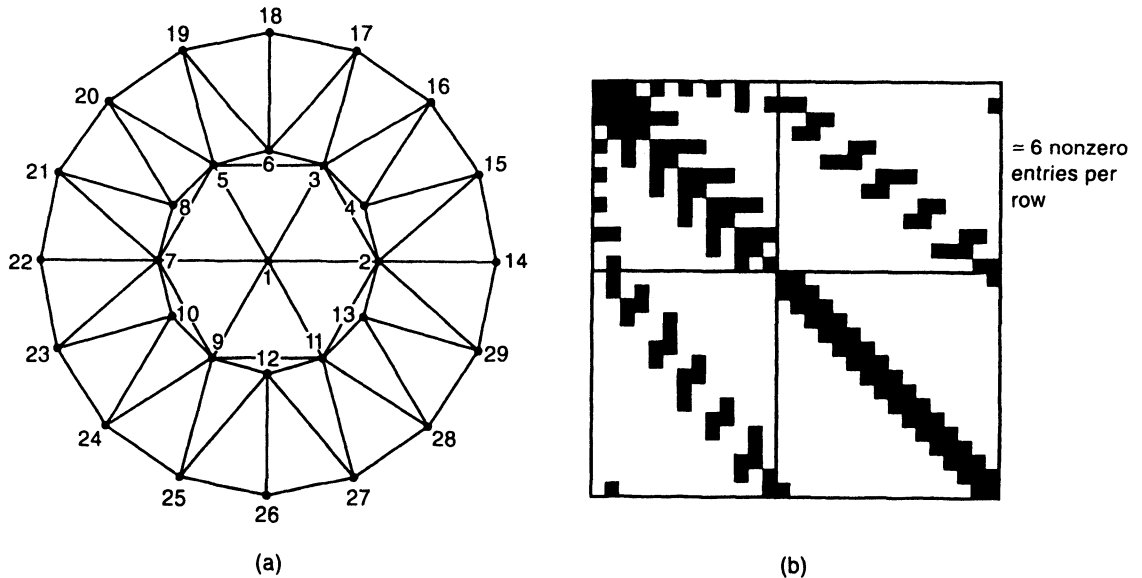


Figure 3.11 Triangular-cell mesh and the associated matrix sparsity pattern obtained with linear pyramid functions and the second-order Bayliss–Turkel RBC.

3.6. The circular conductor has radius $\rho = 0.25\lambda_0$ and is surrounded by a dielectric cladding with $\epsilon_r = 4$ and outer radius $\rho = 0.30\lambda_0$. Tables 3.6 and 3.7 present the two-dimensional scattering cross section as a function of the location of the outer boundary $\partial\Gamma$ for triangular-cell models having 44 nodes on the conductor and two layers of cells in the cladding. These results are compared with the numerical solutions from Tables 3.4 and 3.5, which were obtained using the “exact” eigenfunction RBC. For this example, the TM results are in good agreement with the exact solutions even when $\partial\Gamma$ is located at $\rho = 0.33\lambda_0$ and do not seem very sensitive to the placement of the boundary. The TE results exhibit a larger amount of error for boundary locations close to the scatterer but consistently improve as the boundary radius increases.

TABLE 3.6 Bistatic Scattering Cross Section^a σ_{TM} for Circular Conducting Cylinder with Radius $0.25\lambda_0$ Coated with Dielectric Layer Having $\epsilon_r = 4$ and Outer Radius $0.3\lambda_0$

ϕ (deg)	$\rho = 0.33\lambda_0$	$\rho = 0.37\lambda_0$	$\rho = 0.41\lambda_0$	Exact RBC
0	5.42	5.42	5.40	5.41
30	3.76	3.76	3.76	3.76
60	0.05	0.08	0.10	0.05
90	-1.15	-1.15	-1.15	-1.19
120	-0.78	-0.79	-0.78	-0.74
150	-0.69	-0.68	-0.66	-0.64
180	-0.67	-0.66	-0.65	-0.63

^a In decibels free-space wavelength.

Note: Numerical results obtained using the Bayliss–Turkel RBC located at three different radii are compared with the results obtained using the exact RBC imposed at $\rho = 0.33\lambda_0$.

TABLE 3.7 Bistatic Scattering Cross Section^a σ_{TE} for Circular Conducting Cylinder with Radius $0.25\lambda_0$ Coated with Dielectric Layer Having $\epsilon_r = 4$ and Outer Radius $0.3\lambda_0$

ϕ (deg)	$\rho = 0.33\lambda_0$	$\rho = 0.37\lambda_0$	$\rho = 0.41\lambda_0$	Exact RBC
0	4.43	4.32	4.23	4.17
30	0.12	0.03	-0.04	0.00
60	-1.37	-1.63	-1.76	-1.91
90	1.00	0.94	0.93	1.01
120	-2.51	-2.24	-2.09	-1.87
150	-1.64	-1.71	-1.77	-1.86
180	0.35	0.07	-0.08	-0.10

^a In decibels free-space wavelength.

Note: Numerical results obtained using the Bayliss–Turkel RBC located at three different radii are compared with the results obtained using the exact RBC imposed at $\rho = 0.33\lambda_0$.

As a second example, consider a TE wave incident upon a hollow circular dielectric shell having $\epsilon_r = 4$, inner radius $0.25\lambda_0$, and outer radius $0.30\lambda_0$. Figure 3.12 shows the

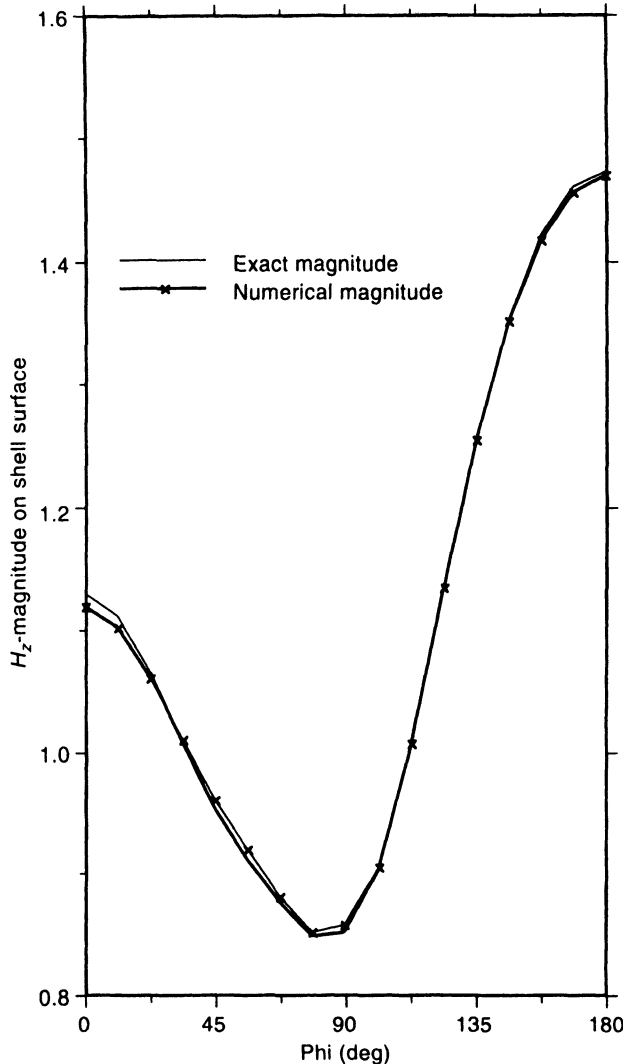


Figure 3.12 The TE magnetic field induced by a uniform plane wave along the surface of a hollow dielectric shell with $\epsilon_r = 4$, $r_{\text{inner}} = 0.25\lambda_0$, and $r_{\text{outer}} = 0.30\lambda_0$.

magnitude of H_z around the outer surface of the cylinder. The numerical result exhibits excellent agreement with the exact analytical solution. The numerical solution was obtained from a 237-node model that employed a single layer of 62 triangular cells to represent the shell. The region inside the shell is discretized into 138 cells, and three exterior layers containing a total of 228 cells are used to place $\partial\Gamma$ at $\rho = 0.42\lambda_0$. The largest cell edge in the entire model has length $0.074\lambda_0$.

Figure 3.13 presents a comparison of numerical solutions for the magnetic field produced on the surface of a homogeneous triangular cylinder with $\epsilon_r = 5$ by an incident TE plane wave. The result from the differential equation formulation incorporating the second-order Bayliss–Turkel RBC is compared with the numerical solution produced by the volume MFIE formulation of Section 2.7 applied to the identical triangular-cell model.

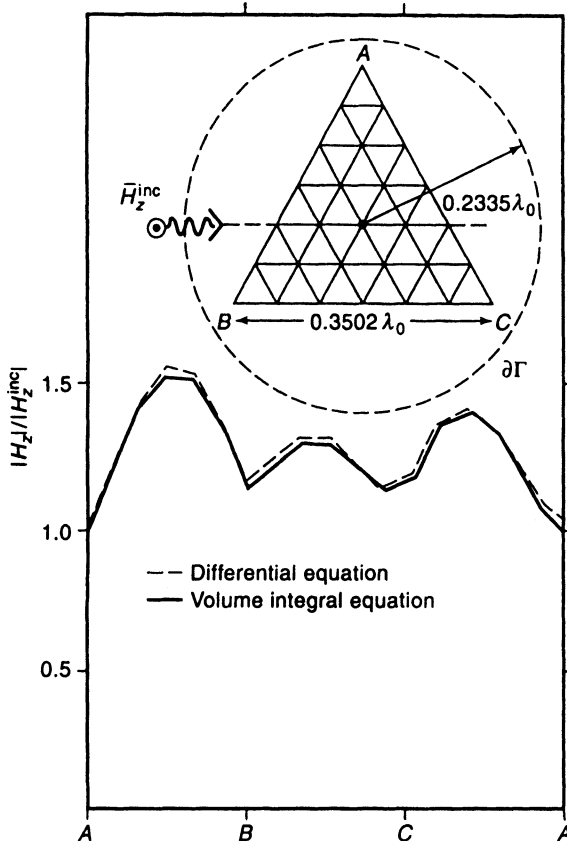


Figure 3.13 The TE magnetic field induced by a uniform plane wave along the surface of a triangular dielectric cylinder with $\epsilon_r = 5$. The radiation boundary is located at radius $0.2335\lambda_0$. The first-order finite-element result is compared to that produced by the volume MFIE of Section 2.7. After [19]. ©1989 VSP BV.

The numerical results are almost indistinguishable, even though the Bayliss–Turkel condition is applied on a boundary $\partial\Gamma$ that almost circumscribes the scatterer. Since the outer boundary is circular, it is necessary to employ additional unknowns with the differential equation formulation to fill the computational domain Γ . However, as compared with the volume integral equation approach, the additional unknowns are offset by a reduction in the overall storage due to the sparsity of the matrix A in (3.88) and a significant reduction in the computational effort required to fill the matrix.

Although the Bayliss–Turkel RBC is approximate, the numerical solutions produced by the differential equation formulation appear reasonably accurate as long as several layers of cells are used to separate the boundary $\partial\Gamma$ from the scatterer surface. While the smattering of results presented in this section does not constitute a comprehensive validation, the high degree of sparsity in the matrix A and the resulting computational efficiency provide strong motivation for the general-purpose use of a local RBC. Additional numerical results illustrating the Bayliss–Turkel RBC will be presented in Section 3.12. A computer program implementing this formulation is described in Appendix D.

Like the eigenfunction RBC developed in Section 3.3, the Bayliss–Turkel condition requires a circular outer boundary $\partial\Gamma$. In an attempt to reduce the overall size of the computational domain, recent work has investigated similar RBCs that can be imposed on general boundary shapes [13, 14]. These conditions are also local and seem to introduce the same level of error as the Bayliss–Turkel RBC. In the following section, we consider more accurate global RBCs that can be imposed on general boundaries.

3.10 EXACT NEAR-ZONE RADIATION BOUNDARY CONDITIONS FOR SURFACES OF GENERAL SHAPE

The formulations presented in Sections 3.4 and 3.9 are restricted to cylinder models that terminate on circular boundaries. While it is always possible in principle to surround a scatterer with a region of free space, an unacceptable number of additional unknowns may be required to extend the computational domain around an elongated geometry (such as an airfoil) out to a circle. In other situations, such as a scatterer in the near field of an antenna, the primary source may be located so close to the scatterer surface that it may not be possible to incorporate a circular boundary. For these situations, alternative radiation boundary conditions can be obtained from surface integral equations. Although these are exact prior to discretization, they suffer from the fact that they are also global conditions and create fill-in beyond that normally associated with the discrete form of a differential operator. However, since they can circumscribe the scatterer without introducing substantial error, these RBCs may sometimes be able to reduce the number of unknowns required with the previous formulations enough to compensate for the additional fill-in.

Radiation boundary conditions can be developed using the surface equivalence principle from Section 1.6. Refer once more to the cylindrical geometry of Figure 3.1, which depicts a scatterer surrounded by a surface $\partial\Gamma$. In the exterior region the total fields can be produced by the superposition of the original “incident” fields and “scattered” fields produced by equivalent secondary sources located on the surface $\partial\Gamma$ and radiating in free space. For the TM polarization, these equivalent sources are

$$J_z = \hat{z} \cdot \hat{n} \times (\hat{i} H_t) = H_t = \frac{1}{jk\eta} \frac{\partial E_z}{\partial n} \quad \text{on } \partial\Gamma \quad (3.97)$$

$$K_t = \hat{i} \cdot (\hat{z} E_z) \times \hat{n} = E_z \quad \text{on } \partial\Gamma \quad (3.98)$$

For the TE polarization, equivalent sources for the scattered fields are

$$J_t = \hat{i} \cdot \hat{n} \times (\hat{z} H_z) = -H_z \quad \text{on } \partial\Gamma \quad (3.99)$$

$$K_z = \hat{z} \cdot (\hat{i} E_t) \times \hat{n} = -E_t = -\frac{j\eta}{k} \frac{\partial H_z}{\partial n} \quad \text{on } \partial\Gamma \quad (3.100)$$

The unit vector \hat{n} is the outward normal vector to the surface, and \hat{i} is the tangent vector defined so that $\hat{n} \times \hat{i} = \hat{z}$. The parameters η and k denote the intrinsic impedance and wavenumber, respectively, of the exterior medium. The equivalent exterior problem is depicted in Figure 3.14.

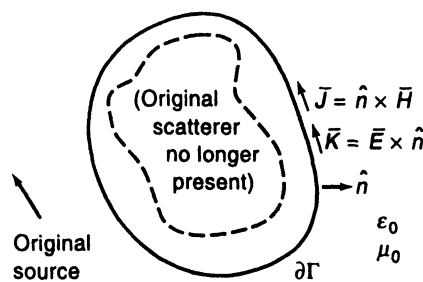


Figure 3.14 Equivalent exterior problem showing equivalent sources located on the radiation boundary $\partial\Gamma$.

The introduction of secondary sources \bar{J} and \bar{K} is merely an intermediate step in the derivation of integral equations. It was shown in Chapters 1 and 2 that the secondary sources

must satisfy the surface EFIE and MFIE (for the TM and TE polarizations, respectively) given by

$$\mathbf{E}_z^{\text{inc}}(t) = \mathbf{K}_t(t) + \hat{\mathbf{z}} \cdot \nabla \times \int_{\partial\Gamma} \bar{\mathbf{K}}_t(t') \frac{1}{4j} \mathbf{H}_0^{(2)}(kR) dt' + jk\eta \int_{\partial\Gamma} \mathbf{J}_z(t') \frac{1}{4j} \mathbf{H}_0^{(2)}(kR) dt' \quad (3.101)$$

$$\mathbf{H}_z^{\text{inc}}(t) = -\mathbf{J}_t(t) - \hat{\mathbf{z}} \cdot \nabla \times \int_{\partial\Gamma} \bar{\mathbf{J}}_t(t') \frac{1}{4j} \mathbf{H}_0^{(2)}(kR) dt' + j\frac{k}{\eta} \int_{\partial\Gamma} \mathbf{K}_z(t') \frac{1}{4j} \mathbf{H}_0^{(2)}(kR) dt' \quad (3.102)$$

where

$$R = \sqrt{[x(t) - x(t')]^2 + [y(t) - y(t')]^2} \quad (3.103)$$

Neither integral equation can uniquely specify both secondary sources, since they incorporate no information describing the interior medium. However, they do provide a direct linear relationship between the equivalent sources and the incident field on $\partial\Gamma$, and this relationship is equivalent to a radiation boundary condition.

A discretization is necessary in order to obtain an explicit radiation condition from the integral equations. Consider the TM polarization and the use of linear pyramid basis functions to represent the interior E_z -field. Since the transverse magnetic field obtained from E_z would be piecewise constant, the boundary discretization compatible with these interior functions would involve piecewise-linear basis functions for K_t and piecewise-constant basis functions for J_z . Simple testing functions, such as Dirac delta functions located in the center of each cell edge around the periphery, can be used to convert Equation (3.101) into the matrix equation

$$\mathbf{e}^{\text{inc}} = \mathbf{L}\mathbf{k}_t + \mathbf{M}\mathbf{j}_z \quad (3.104)$$

where \mathbf{L} and \mathbf{M} are square matrix operators and \mathbf{e}^{inc} , \mathbf{k}_t , and \mathbf{j}_z are column vectors. The details of this type of discretization have been described in Chapter 2. Symbolically, Equation (3.104) is equivalent to

$$\mathbf{j}_z = \mathbf{M}^{-1}\mathbf{e}^{\text{inc}} - \mathbf{M}^{-1}\mathbf{L}\mathbf{k}_t \quad (3.105)$$

which, from an inspection of (3.97) and (3.98), is clearly a linear relationship between the normal derivative of E_z , E_z itself, and E_z^{inc} on $\partial\Gamma$. Except for the discretization, Equation (3.105) has the same form as the exact RBC presented in Equation (3.23). It is somewhat more general than (3.23), however, since the shape of the boundary is not restricted. [To be precise, the equation relates coefficients of basis functions to sampled values of the incident field. However, as long as the discretization of (3.101) is compatible with that of the Helmholtz equation, the distinction is of no consequence.]

To illustrate the implementation of the integral equation RBC, consider the weak scalar Helmholtz equation in (3.5), which can be rewritten in the form

$$\iint_{\Gamma} \left(\frac{1}{\mu_r} \nabla T \cdot \nabla E_z - k^2 \epsilon_r T E_z \right) dx dy = j\omega\mu_0 \int_{\partial\Gamma} T \mathbf{J}_z dt \quad (3.106)$$

where \mathbf{J}_z is the equivalent surface current density defined in (3.97). The interior field can be expanded in basis functions

$$E_z(x, y) \cong \sum_{n=1}^{N_{\text{int}}} e_{zn}^{\text{int}} B_n(x, y) + \sum_{n=N_{\text{int}}+1}^{N_{\text{int}}+N_{\text{bound}}} e_{zn}^{\text{bound}} B_n(x, y) \quad (3.107)$$

where N_{int} is the number of interior unknowns and N_{bound} is the number of unknowns located

on the radiation boundary $\partial\Gamma$. The equivalent surface current J_z can be expressed as

$$J_z(t) \cong \sum_{n=1}^{N_{\text{bound}}} j_{zn} \tilde{B}_n(t) \quad (3.108)$$

where t is a parametric variable along $\partial\Gamma$ and \tilde{B} may be a different basis function than B . Since $E_z = K_t$ by (3.98), the magnetic surface current density is automatically given by

$$K_t(t) \cong \sum_{n=N_{\text{int}}+1}^{N_{\text{int}}+N_{\text{bound}}} e_{zn}^{\text{bound}} B_n(t) \quad (3.109)$$

where $B_n(t)$ is the projection of $B_n(x, y)$ onto the boundary. Therefore, prior to imposing a radiation condition, the discretized weak equation can be written as

$$\begin{bmatrix} \mathbf{I} & \mathbf{I}_b^T & \mathbf{0} \\ \mathbf{I}_b & \mathbf{E} & \mathbf{J} \end{bmatrix} \begin{bmatrix} \mathbf{e}_z^{\text{int}} \\ \mathbf{e}_z^{\text{bound}} \\ \mathbf{j}_z \end{bmatrix} = \begin{bmatrix} \mathbf{0} \\ \mathbf{0} \end{bmatrix} \quad (3.110)$$

where the entries of \mathbf{I} , \mathbf{I}_b , and \mathbf{E} represent interior interactions and have the common form

$$I_{mn} = \iint_{\Gamma} \frac{1}{\mu_r} \nabla B_m \cdot \nabla B_n - k^2 \epsilon_r B_m B_n \quad (3.111)$$

and the entries of \mathbf{J} can be expressed as

$$J_{mn} = -j\omega\mu_0 \int_{\partial\Gamma} B_m \tilde{B}_n \quad (3.112)$$

Finally, the RBC of (3.105) can be substituted for \mathbf{j}_z to produce

$$\begin{bmatrix} \mathbf{I} & \mathbf{I}_b^T \\ \mathbf{I}_b & \mathbf{E} - \mathbf{JM}^{-1}\mathbf{L} \end{bmatrix} \begin{bmatrix} \mathbf{e}_z^{\text{int}} \\ \mathbf{e}_z^{\text{bound}} \end{bmatrix} = \begin{bmatrix} \mathbf{0} \\ -\mathbf{JM}^{-1}\mathbf{e}^{\text{inc}} \end{bmatrix} \quad (3.113)$$

Equation (3.113) constitutes an outward-looking formulation that can be solved for the coefficients of the E_z -field throughout the computational domain. The blocks of the matrix containing \mathbf{I} , \mathbf{I}_b , and \mathbf{I}_b^T are sparse, while the block $\mathbf{E} - \mathbf{JM}^{-1}\mathbf{L}$ (the submatrix associated with nodes on $\partial\Gamma$) is fully populated. The basic structure of the global finite-element system is similar to that shown in Figure 3.5.

In this formulation, the number of unknown coefficients is equal to the number of unconstrained nodes in the mesh (for the TM case, all nodes not located on conducting boundaries). Because the surface integral equation is an “exact” RBC prior to discretization, the error arising within this procedure should be comparable to that of the formulation discussed in Section 3.4. Applications of this type of approach are described in the literature [15, 16], and we refer the reader to these references for examples.

Two principal drawbacks associated with the preceding formulation are the full submatrices arising from the global nature of the RBC and the need to construct the inverse of \mathbf{M} as the first step of the procedure (at the least, \mathbf{M}^{-1} must be constructed implicitly in terms of an LU factorization; see Chapter 4). The initial inversion of \mathbf{M} can be avoided by using Equation (3.104) instead of (3.105), at the expense of additional unknowns representing J_z on $\partial\Gamma$. The latter approach is equivalent to the simultaneous solution of (3.104) and (3.110) and constitutes an alternative formulation [17]. However, because (3.104) contains two full matrices, and since the combination of (3.104) and (3.110) will produce a larger

order matrix than (3.113) because of the additional unknowns, the alternative formulation does not appear to offer a savings in either storage or computation when compared with (3.113).

3.11 CONNECTION BETWEEN THE SURFACE INTEGRAL AND EIGENFUNCTION RBCS

The exact RBC developed in Section 3.3 can also be obtained from a surface integral equation, and we illustrate the alternative derivation in order to conceptually connect the integral equation and eigenfunction expansion ideas. As discussed in the preceding section, (3.105) constitutes an integral equation RBC but involves a numerical inversion to obtain M^{-1} . If the boundary $\partial\Gamma$ is circular, however, an exact radiation condition may be developed without the need to numerically invert the integral operator. Consider the TM polarization and Equation (3.101). Assuming that $\partial\Gamma$ is circular with radius a , that the unknown functions are expanded in cylindrical harmonics according to

$$J_z(\phi) \cong \sum_{n=-M}^M j_n e^{jn\phi} \quad (3.114)$$

$$K_t(\phi) \cong \sum_{n=-M}^M k_n e^{jn\phi} \quad (3.115)$$

and that Equation (3.101) is enforced on the circular boundary by integrating over ϕ with testing functions $e^{-jn\phi}$, the result is an $N \times 2N$ matrix equation (where $N = 2M + 1$) of the form

$$\begin{bmatrix} \alpha_{-M} & 0 & \cdots & 0 & \beta_{-M} & 0 & \cdots & 0 \\ 0 & \alpha_{1-M} & & 0 & 0 & \beta_{1-M} & & 0 \\ \cdot & \cdot \\ \cdot & \cdot \\ \cdot & \cdot \\ 0 & 0 & \cdots & \alpha_M & 0 & 0 & \cdots & \beta_M \end{bmatrix} \begin{bmatrix} j_{-M} \\ \vdots \\ j_M \\ k_{-M} \\ \vdots \\ k_M \end{bmatrix} = \begin{bmatrix} e_{-M} \\ \vdots \\ e_M \end{bmatrix} \quad (3.116)$$

By carrying out the usual integrations over the basis and testing functions (Prob. P3.21), the diagonal elements of Equation (3.116) are found to be

$$\alpha_n = \frac{1}{2}(\eta\pi ka) J_n(ka) H_n^{(2)}(ka) \quad (3.117)$$

$$\beta_n = \frac{1}{2}(j\pi ka) J_n(ka) H_n^{(2)\prime}(ka) \quad (3.118)$$

and the right-hand side is given by

$$e_n = \frac{1}{2\pi} \int_0^{2\pi} E_z^{\text{inc}}(\phi) e^{-jn\phi} d\phi \quad (3.119)$$

The prime in Equation (3.118) denotes differentiation with respect to the argument of the Hankel function.

A similar development follows for the TE polarization, incorporating the expansions

$$J_t(\phi) \cong \sum_{n=-M}^M j_n e^{jn\phi} \quad (3.120)$$

$$K_z(\phi) \cong \sum_{n=-M}^M k_n e^{jn\phi} \quad (3.121)$$

to discretize Equation (3.102). Enforcing the equation with testing functions $e^{-jn\phi}$ produces the system

$$\begin{bmatrix} \alpha_{-M} & 0 & \cdots & 0 & \beta_{-M} & 0 & \cdots & 0 \\ 0 & \alpha_{1-M} & & 0 & 0 & \beta_{1-M} & & 0 \\ \cdot & \cdot \\ \cdot & \cdot \\ \cdot & \cdot \\ 0 & 0 & \cdots & \alpha_M & 0 & 0 & \cdots & \beta_M \end{bmatrix} \begin{bmatrix} j_{-M} \\ \vdots \\ j_M \\ k_{-M} \\ \vdots \\ k_M \end{bmatrix} = \begin{bmatrix} h_{-M} \\ \vdots \\ h_M \end{bmatrix} \quad (3.122)$$

where

$$\alpha_n = -\frac{1}{2}(j\pi ka) J_n(ka) H_n^{(2)\prime}(ka) \quad (3.123)$$

$$\beta_n = \frac{\pi ka}{2\eta} J_n(ka) H_n^{(2)}(ka) \quad (3.124)$$

and

$$h_n = \frac{1}{2\pi} \int_0^{2\pi} H_z^{\text{inc}}(\phi) e^{-jn\phi} d\phi \quad (3.125)$$

In contrast to the fully populated matrices encountered in Chapter 2, Equations (3.116) and (3.122) contain nonzero entries only on the main and minor diagonals. The diagonal nature of these matrices is a consequence of employing the eigenfunctions of the integral operators as basis and testing functions, which is usually only practical for boundaries $\partial\Gamma$ that are separable (i.e., circular or elliptical). For other surface shapes or other basis or testing functions, the systems would generally be fully populated [18].

Since the matrices are diagonal, the inversion necessary to cast these equations into the form of a radiation boundary condition is easily carried out analytically. Consider the TM polarization and one of the individual equations from (3.116), which can be written

$$\alpha_n j_n + \beta_n k_n = e_n \quad (3.126)$$

where α_n and β_n have been defined in (3.117) and (3.118),

$$j_n = \frac{1}{2\pi} \int_0^{2\pi} J_z(\phi') e^{-jn\phi'} d\phi' \quad (3.127)$$

$$k_n = \frac{1}{2\pi} \int_0^{2\pi} K_t(\phi') e^{-jn\phi'} d\phi' \quad (3.128)$$

and e_n is defined in (3.119). Solving Equation (3.126) for j_n , we rewrite (3.114) in the form

$$J_z(\phi) = \sum_{n=-\infty}^{\infty} \frac{e_n - \beta_n k_n}{\alpha_n} e^{jn\phi} \quad (3.129)$$

By replacing the Fourier coefficients e_n and k_n by their explicit integral representation and exchanging the order of integration and summation, we obtain the RBC previously given in Equation (3.23). A similar procedure can be carried out for the TE polarization.

The equivalence between the surface integral equation RBC and the RBC obtained in Section 3.3 is a simple consequence of the inherent connection between the cylindrical eigenfunction expansion and the integral equation representations. Although the former is restricted in practice to situations where the boundaries conform to separable surfaces, the two descriptions are conceptually equivalent.

3.12 INWARD-LOOKING DIFFERENTIAL EQUATION FORMULATION: THE UNIMOMENT METHOD

Preceding sections have presented *outward-looking* formulations for combining the scalar Helmholtz equations with radiation boundary conditions. These approaches employ an RBC to augment the Helmholtz equation, producing a formulation in which the primary unknown is the E_z - or H_z -field throughout Γ . We now consider a complementary approach where the equation representing the interior problem is used to constrain equivalent sources located on $\partial\Gamma$ and representing the exterior problem. Since the primary unknowns in this formulation are coefficients of equivalent sources on the outer boundary, as would be “seen” by an observer standing outside the region Γ and looking in, we denote this as an *inward-looking* formulation [6].

The starting point in this inward-looking formulation is the relationship embodied in Equations (3.116) and (3.122). Recall that these equations provide a description of the exterior scattering problem in terms of \bar{J} and \bar{K} located on the boundary but contain no information about the interior medium. What is needed is an additional equation relating \bar{J} and \bar{K} to the interior problem. In fact, such a relationship is provided by the scalar Helmholtz equations in (3.1) and (3.2) or their weak forms in (3.5) and (3.6). Consider the TM polarization. Knowledge of K_t on the boundary is equivalent to a Dirichlet boundary condition for E_z . Given K_t on the entire boundary, Equation (3.5) uniquely describes the interior E_z -field. After E_z is determined, the associated J_z could be constructed from the normal derivative of the E_z -field on the surface. Similarly, if J_z is prescribed on the entire boundary, Equation (3.5) can be solved subject to the equivalent Neumann boundary condition to produce a corresponding K_t . Thus, Equation (3.5) can be used to provide a linear relationship between J_z and K_t , which can be combined with Equation (3.116) to determine the secondary sources.

To construct a secondary $N \times 2N$ system providing the linear relationship between the unknowns J_z and K_t , consider the repeated finite-element solution of Equation (3.5) subject to the Neumann boundary condition

$$\frac{\partial E_z}{\partial \rho} = jk\eta e^{jm\phi} \quad \text{on } \partial\Gamma \quad (3.130)$$

which is equivalent to

$$J_z = e^{jm\phi} \quad (3.131)$$

In common with the preceding formulations, we divide the region Γ into triangular cells of constant permittivity and permeability, as depicted in Figure 3.3, and represent E_z by subsectional linear interpolation (“pyramid”) functions

$$E_z(x, y) \cong \sum_{q=1}^N e_q B_q(x, y) \quad (3.132)$$

where $B_q(x, y)$ denotes a basis function centered at node q . If this expression is substituted into Equation (3.5), N linearly independent equations can be generated using

$$T(x, y) = B_p(x, y) \quad p = 1, 2, \dots, N \quad (3.133)$$

The resulting matrix equation has the form

$$\mathbf{A}\mathbf{e} = \mathbf{b} \quad (3.134)$$

with entries given by

$$A_{pq} = \iint_{\Gamma} \left(\frac{1}{\mu_r} \nabla B_p \cdot \nabla B_q - k^2 \epsilon_r B_p B_q \right) dx dy \quad (3.135)$$

and

$$b_p = jk\eta \int_{\partial\Gamma} B_p e^{jm\phi} \rho d\phi \quad (3.136)$$

Because the interaction between the basis and testing functions is entirely local, \mathbf{A} is a sparse matrix. Since the boundary contributions are also local, the sparsity pattern in \mathbf{A} is comparable to that illustrated in Figure 3.11 (i.e., that associated with the outward-looking formulation employing the Bayliss–Turkel radiation condition).

After Equation (3.134) is solved to produce values of E_z throughout Γ , the fields on the boundary $\partial\Gamma$ can be decomposed into the expansion functions $e^{jn\phi}$ to produce

$$E_z(\phi) \cong \sum_{n=-M}^M \gamma_{n,m} e^{jn\phi} \cong K_t(\phi) \quad (3.137)$$

where

$$\gamma_{n,m} = \frac{1}{2\pi} \int_0^{2\pi} E_z(\phi) e^{-jn\phi} d\phi \quad (3.138)$$

This process of solving the matrix equation and decomposing the boundary fields must be repeated for each harmonic retained in the expansion of Equations (3.114) and (3.115). The linear relationship between the coefficients of J_z and K_t follows from the fact that an arbitrary Neumann condition

$$J_z(\phi) \cong \sum_{m=-M}^M j_m e^{jm\phi} \quad (3.139)$$

would produce the boundary expansion

$$K_t(\phi) \cong \sum_{n=-M}^M \sum_{m=-M}^M \gamma_{n,m} j_m e^{jn\phi} \quad (3.140)$$

Equating this expansion with (3.115), that is,

$$K_t(\phi) \cong \sum_{n=-M}^M k_n e^{jn\phi} \quad (3.141)$$

yields the $N \times 2N$ system

$$\begin{bmatrix} \gamma_{-M,-M} & \gamma_{-M,1-M} & \cdots & \gamma_{-M,M} & -1 & 0 & \cdots & 0 \\ \gamma_{1-M,-M} & \gamma_{1-M,1-M} & \cdots & \gamma_{1-M,M} & 0 & -1 & \cdots & 0 \\ \vdots & \vdots & \ddots & \vdots & \vdots & \vdots & \ddots & \vdots \\ \vdots & \vdots & \ddots & \vdots & \vdots & \vdots & \ddots & \vdots \\ \gamma_{M,-M} & \gamma_{M,1-M} & \cdots & \gamma_{M,M} & 0 & 0 & \cdots & -1 \end{bmatrix} \begin{bmatrix} j_{-M} \\ \vdots \\ j_M \\ k_{-M} \\ \vdots \\ k_M \end{bmatrix} = \begin{bmatrix} 0 \\ 0 \\ \vdots \\ \vdots \\ 0 \end{bmatrix} \quad (3.142)$$

Equation (3.142) is a matrix description of the relationship between E_z and its normal derivative on the interior side of the boundary $\partial\Gamma$ and takes into account the effects of the inhomogeneous material in the region Γ . The relationship of the boundary fields to the incident field is provided by Equation (3.116). Together, Equations (3.116) and (3.142) comprise a $2N \times 2N$ matrix description of the scattering problem. Once this matrix is constructed for a given cylinder geometry, any number of different incident fields may be treated by solving the system for additional right-hand sides. Since three of the four blocks of the $2N \times 2N$ system are diagonal, it can be reduced to a fully populated $N \times N$ matrix for computational purposes.

The TE polarization can be treated in a similar fashion using Equation (3.6) and working with the magnetic field H_z instead of the electric field [19]. (As an alternative to the above scheme, applied Dirichlet boundary conditions can be used with either the TM or TE polarization instead of Neumann conditions. The general procedure remains the same. However, if Dirichlet conditions are employed, the approximate differentiation process necessary to construct the other source may introduce additional error into the results.)

In summary, this inward-looking formulation requires the solution of the sparse finite-element system representing the interior problem for the $2M - 1$ right-hand sides required to construct (3.142). The $2N \times 2N$ system obtained from Equations (3.116) and (3.142) can be solved to produce the equivalent sources \bar{J} and \bar{K} . These sources can be used directly to produce the far fields. If the interior field distribution is required, the finite-element system must be solved one additional time using either \bar{J} or \bar{K} as an applied boundary condition.

The accuracy of the inward-looking formulation is comparable to that of the outward-looking formulations of the preceding sections. As an example, consider a layered dielectric cylinder having a core region with $\epsilon_r = 10 - j5$ and radius $\rho = 0.0939\lambda_0$ surrounded by a cladding with $\epsilon_r = 6$ and $\rho = 0.15\lambda_0$. Several numerical results for the internal electric field induced by an incident TE wave are compared with exact solutions in Figure 3.15. For this example, H_z is represented by piecewise-linear functions. The transverse electric field is obtained by differentiation and is therefore piecewise constant. The inward-looking differential equation result is virtually identical with the MFIE result (Section 2.7) obtained from the same 75-node model, and both exhibit excellent agreement with the exact solution. (The model employed 42 cells to represent the core region, 38 to represent the cladding,

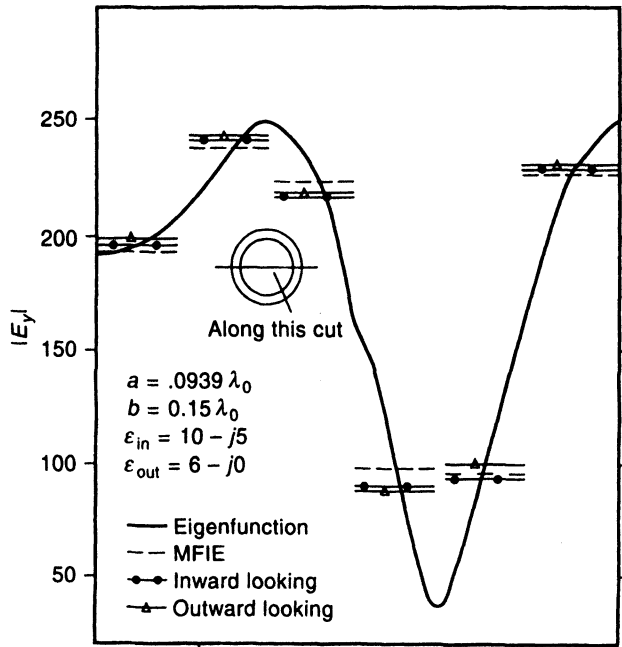


Figure 3.15 The TE electric field within a layered dielectric cylinder. Results from the inward-looking finite-element approach, the outward-looking approach using the second-order Bayliss-Turkel RBC, and the volume MFIE formulation of Section 2.7 are compared with the exact solution. The outward-looking result incorporating the Bayliss-Turkel RBC is obtained with the radiation boundary located at radius $0.41\lambda_0$. After [19]. ©1989 VSP BV.

and an additional layer of 44 cells outside the cylinder to place the outer boundary at $\rho = 0.23\lambda_0$.) The result from the outward-looking formulation using the second-order Bayliss-Turkel radiation boundary condition is also shown and is almost identical with the other numerical solutions. (Three layers of cells outside the scatterer were used in order to locate the Bayliss-Turkel boundary at $\rho = 0.41\lambda_0$.) Similar results from the numerical methods are shown in Figure 3.16 for a cylinder model with a greater density of cells. In Figure 3.16, the outer boundary on which the approximate Bayliss-Turkel condition is applied is brought in closer to the surface of the dielectric scatterer, resulting in some additional error in that result. Table 3.8 compares the scattering cross section data produced by the inward-looking formulation for these two models with the exact solution. An eigenfunction expansion procedure similar to that described in Equations (3.39)–(3.41) was used to calculate σ_{TE} . The numerical results appear to be converging toward the exact solution as the model is refined.

As an additional example, consider a lossy circular dielectric cylinder of radius $0.0179\lambda_0$ and relative permittivity $\epsilon_r = 75 - j300$ illuminated by a TE wave. Numerical and exact results for this scatterer are presented in Figure 3.17. Although the relative permittivity is quite large, results suggest that the inward-looking formulation of this section, the outward-looking formulation employing the second-order Bayliss-Turkel RBC, and the volume MFIE formulation of Section 2.7 all produce stable, accurate solutions. In fact, the results from the inward-looking and outward-looking formulations are essentially identical.

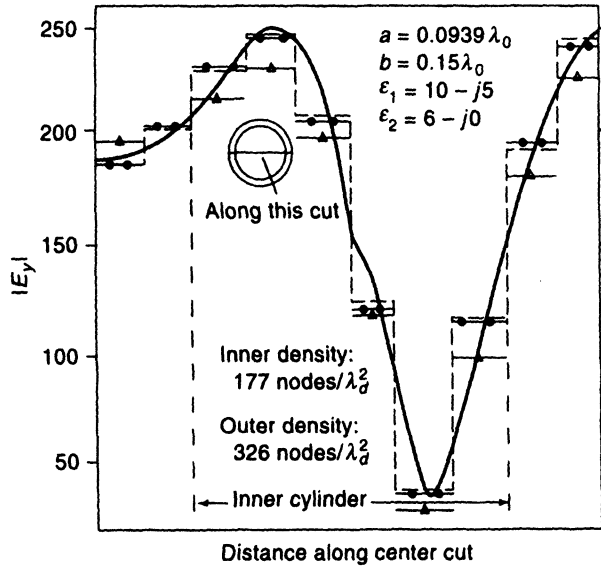


Figure 3.16 The TE electric field produced within the layered dielectric cylinder of Figure 3.15 for a finer triangular-cell model. (—) exact; (---) MFIE (Section 2.7); (●) inward-looking PDE (Section 3.12); (Δ) outward-looking PDE with Bayliss-Turkel RBC (Section 3.9) applied at $\rho = 0.25\lambda_0$. After [19]. ©1989 VSP BV.

TABLE 3.8 Bistatic Scattering Cross Section^a σ_{TE} for a Circular Dielectric Cylinder with Radius $0.0939\lambda_0$ and $\epsilon_r = 10 - j5$ Coated with Dielectric Layer Having $\epsilon_r = 6$ and Outer Radius $0.15\lambda_0$

ϕ (deg)	75-Node	151-Node	Exact
0	0.83	1.08	1.102
30	-0.22	0.02	0.044
60	-3.21	-3.05	-3.059
90	-6.60	-6.74	-6.814
120	-6.77	-6.79	-6.801
150	-5.51	-5.24	-5.157
180	-5.02	-4.65	-4.544

^a In decibels free-space wavelength.

Note: Numerical results obtained with the two cylinder models used in Figures 3.15 and 3.16 are compared with the exact solution.

There are several advantages to the inward-looking formulation compared with the outward-looking formulation of Section 3.4. Because of the global RBC, the finite-element system of Equation (3.30) is not as sparse as that of Equation (3.134). In addition, if the scatterer is lossless, (3.134) involves a real-symmetric matrix as opposed to the complex-valued system of (3.30). Consequently, the inward-looking formulation will generally require less storage than (3.30). Although the outward-looking formulation employing the Bayliss-Turkel condition (Section 3.9) has sparsity that is comparable to this inward-looking approach, that scheme employs an approximate radiation condition that may introduce additional error into the solution or involve additional unknowns because of the need to locate the radiation boundary relatively far from the scatterer surface. The matrix arising in that formulation is also complex valued.

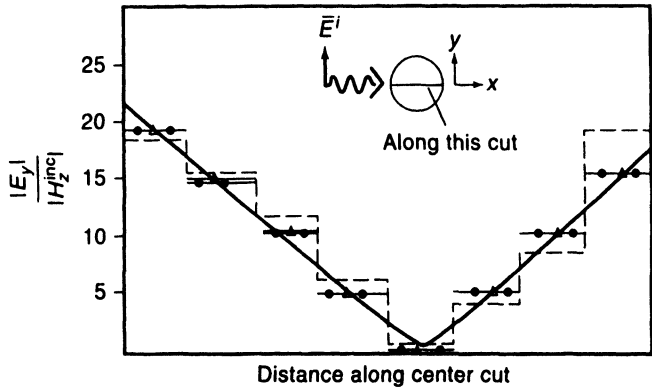


Figure 3.17 The TE electric field within a homogeneous dielectric cylinder with radius $0.0179\lambda_0$ and $\epsilon_r = 75 - j300$. Results from the inward-looking finite-element approach, the outward-looking approach using the second-order Bayliss-Turkel RBC, and the volume MFIE formulation of Section 2.7 are compared with the exact solution: (—) exact; (- - -) MFIE; (●) inward looking; (Δ) outward looking. The outward-looking result incorporating the Bayliss-Turkel RBC is obtained with the radiation boundary located at radius $0.032\lambda_0$. After [19]. ©1989 VSP BV.

There are also disadvantages to the inward-looking approach. Because of the need to solve (3.134) repeatedly and decompose the boundary fields according to Equation (3.137), there is additional computational overhead not encountered in the outward-looking approaches. Another drawback to the inward-looking formulation is that the interior problem is being modeled as a closed region. Even if some loss is present, the system of equations may be nearly singular if the surface $\partial\Gamma$ happens to coincide with the surface of a resonant cavity. (This difficulty is explored in Chapter 6.) For electrically large domains, the cavity resonances may be difficult to avoid. In the outward-looking formulations, however, radiation loss eliminates the resonances and ensures that the system of equations is nonsingular.

Although presented from a different point of view, the formulation described in this section is equivalent to the *unimoment method* discussed in the literature [20, 21]. It is also possible to generalize this approach in order to employ an arbitrarily shaped boundary by using a surface integral equation to relate \bar{J} and \bar{K} on $\partial\Gamma$ to the incident field through the exterior medium. The discretization of the integral equation produces a fully populated matrix equation that takes the place of Equation (3.116). The interior problem is then solved as described above using the basis functions employed with the surface integral equation as the applied excitation instead of the exponential functions of (3.114) and (3.115). The result is a second fully populated system replacing Equation (3.142). Additional implementation details are available in several recent articles [22–24].

3.13 SUMMARY

This chapter has introduced several differential equation formulations for electromagnetic scattering from two-dimensional targets. The computational domain associated with these approaches must be truncated with a radiation boundary condition, and the primary focus

of this chapter has been to investigate several near-field RBCs and explore various ways of incorporating them into the formulation. The inward-looking formulation of Section 3.12 requires that a large finite-element system be solved in order to construct a smaller fully populated matrix equation representing the scatterer. In contrast, the outward-looking approaches developed in the previous sections of this chapter permit the treatment of the scattering problem with a single finite-element system. The sparse nature of the finite-element system is degraded by the fill-in resulting from the global nature of any exact near-field radiation condition. Approximate local radiation conditions, such as the Bayliss-Turkel RBC, alleviate the fill-in problem but may introduce some inaccuracy.

Details have been provided to illustrate the finite-element discretization of the scalar Helmholtz equation and the associated boundary integrals using first-order linear interpolation functions on triangular cells. An analysis of discretization error (carried out in Chapter 5) suggests that linear basis functions limit the accuracy for electrically large regions. To produce greater accuracy, higher order interpolation functions and cells having an arbitrary shape will be considered in Chapter 9.

As compared to the integral equation formulations considered in Chapter 2, the primary computational advantage of the differential equation approaches is the resulting matrix sparsity. Algorithms that exploit this sparsity during the solution of the system of equations are the focus of Chapter 4.

REFERENCES

- [1] J. N. Reddy, *An Introduction to the Finite Element Method*, New York: McGraw-Hill, 1984.
- [2] G. Strang and G. J. Fix, *An Analysis of the Finite Element Method*, Englewood Cliffs, NJ: Prentice-Hall, 1973.
- [3] R. B. Wu and C. H. Chen, "Variational reaction formulation of scattering problem for anisotropic dielectric cylinders," *IEEE Trans. Antennas Propagat.*, vol. 34, pp. 640–645, May 1986.
- [4] L. W. Pearson, R. A. Whitaker, and L. J. Bahrmasel, "An exact radiation boundary condition for the finite-element solution of electromagnetic scattering on an open domain," *IEEE Trans. Magnet.*, vol. 25, pp. 3046–3048, July 1989.
- [5] R. F. Harrington, *Time-Harmonic Electromagnetic Fields*, New York: McGraw-Hill, 1961.
- [6] L. W. Pearson, A. F. Peterson, L. J. Bahrmasel, and R. A. Whitaker, "Inward-looking and outward-looking formulations for scattering from penetrable objects," *IEEE Trans. Antennas Propagat.*, vol. 40, pp. 714–720, June 1992.
- [7] P. P. Silvester and R. L. Ferrari, *Finite Elements for Electrical Engineers*, Cambridge: Cambridge University Press, 1983.
- [8] A. F. Peterson and S. P. Castillo, "Differential equation methods for electromagnetic scattering from inhomogeneous cylinders," in *Radar Cross Sections of Complex Objects*, ed. W. R. Stone, New York: IEEE Press, 1990.
- [9] A. Bayliss and E. Turkel, "Radiation boundary conditions for wave-like equations," *Comm. Pure Appl. Math.*, vol. 33, pp. 707–725, 1980.
- [10] F. X. Canning, "On the application of some radiation boundary conditions," *IEEE Trans. Antennas Propagat.*, vol. 38, pp. 740–745, May 1990.

- [11] R. Mittra and O. Ramahi, "Absorbing boundary conditions for the direct solution of partial differential equations arising in electromagnetic scattering problems," in *Finite Element and Finite Difference Methods in Electromagnetic Scattering*, ed. M. A. Morgan, New York: Elsevier, 1990.
- [12] A. F. Peterson and S. P. Castillo, "A frequency-domain differential equation formulation for electromagnetic scattering from inhomogeneous cylinders," *IEEE Trans. Antennas Propagat.*, vol. AP-37, pp. 601–607, May 1989.
- [13] G. A. Kriegsmann, A. Taflove, and K. R. Umashankar, "A new formulation of electromagnetic wave scattering using an on-surface radiation boundary condition approach," *IEEE Trans. Antennas Propagat.*, vol. 35, pp. 153–161, Feb. 1987.
- [14] B. Lichtenberg, K. J. Webb, D. B. Meade, and A. F. Peterson, "Comparison of two-dimensional conformable local radiation boundary conditions," *Electromagnetics*, vol. 16, pp. 359–384, 1996.
- [15] B. H. McDonald and A. Wexler, "Finite element solution of unbounded field problems," *IEEE Trans. Microwave Theory Tech.*, vol. MTT-20, pp. 841–847, Dec. 1972.
- [16] S. P. Marin, "Computing scattering amplitudes for arbitrary cylinders under incident plane waves," *IEEE Trans. Antennas Propagat.*, vol. AP-30, pp. 1045–1049, Nov. 1982.
- [17] Z. Gong and A. W. Glisson, "A hybrid approach for the solution of electromagnetic scattering problems involving two-dimensional inhomogeneous dielectric cylinders," *IEEE Trans. Antennas Propagat.*, vol. 38, pp. 60–68, Jan. 1990.
- [18] R. F. Harrington, *Field Computation by Moment Methods*, Malabar, FL: Krieger, 1982.
- [19] A. F. Peterson, "A comparison of integral, differential, and hybrid methods for TE-wave scattering from inhomogeneous dielectric cylinders," *J. Electromagnetic Waves Appl.*, vol. 3, pp. 87–106, 1989.
- [20] K. K. Mei, "Unimoment method for solving antenna and scattering problems," *IEEE Trans. Antennas Propagat.*, vol. AP-22, pp. 760–766, Nov. 1974.
- [21] S. K. Chang and K. K. Mei, "Application of the unimoment method to electromagnetic scattering by dielectric cylinders," *IEEE Trans. Antennas Propagat.*, vol. AP-24, pp. 35–42, Jan. 1976.
- [22] J. M. Jin and V. V. Liepa, "A note on hybrid finite element method for solving scattering problems," *IEEE Trans. Antennas Propagat.*, vol. AP-36, pp. 1486–1490, Oct. 1988.
- [23] X. Yuan, D. R. Lynch, and J. W. Strohbehn, "Coupling of finite element and moment methods for electromagnetic scattering from inhomogeneous objects," *IEEE Trans. Antennas Propagat.*, vol. AP-38, pp. 386–393, March 1990.
- [24] A. C. Cangellaris and R. Lee, "The bymoment method for two-dimensional electromagnetic scattering," *IEEE Trans. Antennas Propagat.*, vol. AP-38, pp. 1429–1437, Sept. 1990.

PROBLEMS

P3.1 Beginning with Maxwell's equations, generalize Equation (3.1) to include sources J_z and K , located in the region Γ .

P3.2 Finite-element formulations are often based on direct variational methods, that is, finding the stationary point of a functional. Consider the functional

$$F(\Psi) = \frac{1}{2} \iint_{\Gamma} \left(\frac{1}{\mu_r} \nabla \Psi \cdot \nabla \Psi - k^2 \epsilon_r \Psi^2 \right) dx dy$$

and a trial solution $\Psi = E_z + \epsilon \Phi$. The function E_z satisfies the scalar Helmholtz equation

$$\nabla \cdot \left(\frac{1}{\mu_r} \nabla E_z \right) + k^2 \epsilon_r E_z = 0$$

subject to specified Dirichlet boundary conditions along some portion of the boundary $\partial\Gamma$ and homogeneous Neumann boundary conditions along the rest of $\partial\Gamma$. The function $\Phi(x, y)$ vanishes on the portion of $\partial\Gamma$ over which Dirichlet conditions are specified and ϵ is a scalar parameter.

By direct substitution and the use of Equations (3.3) and (3.4), show that

$$F(\Psi) - F(E_z) = O(\epsilon^2) \quad \text{as } \epsilon \rightarrow 0$$

and therefore the functional F has a stationary point at $\Psi = E_z$.

P3.3 (a) Problem P3.2 demonstrated that the quadratic functional

$$F(E_z) = \frac{1}{2} \iint_{\Gamma} \left(\frac{1}{\mu_r} \nabla E_z \cdot \nabla E_z - k^2 \epsilon_r (E_z)^2 \right) dx dy$$

is stationary about the solution to the scalar Helmholtz equation

$$\nabla \cdot \left(\frac{1}{\mu_r} \nabla E_z \right) + k^2 \epsilon_r E_z = 0$$

for the case of Dirichlet boundary conditions or homogeneous Neumann boundary conditions on $\partial\Gamma$. Assume that the unknown field is expanded in basis functions

$$E_z(x, y) \cong \sum_{n=1}^N e_n B_n(x, y) + \sum_{n=N+1}^M e_n B_n(x, y)$$

where $\{e_n\}$, $n = 1, 2, \dots, N$ are *unknown* coefficients and $\{e_n\}$, $n = N+1, N+2, \dots, M$ are *known* coefficients chosen to satisfy the Dirichlet boundary conditions on $\partial\Gamma$. By differentiating the functional with respect to each of the first N coefficients $\{e_n\}$, obtain a matrix equation for $\{e_n\}$.

- (b) How does this equation compare to that arising from the weak equation (3.5) if the same functions are used as basis functions and testing functions to discretize the weak equation?
- (c) Consider the incorporation of nonhomogeneous Neumann boundary conditions. Assume that the expansion has the form

$$E_z(x, y) \cong \sum_{n=1}^N e_n B_n(x, y) + \sum_{n=N+1}^M e_n B_n(x, y) + \sum_{n=M+1}^P e_n B_n(x, y)$$

where $\{e_n\}$, $n = 1, 2, \dots, N$ are *unknown* coefficients associated with interior bases, $\{e_n\}$, $n = N+1, N+2, \dots, M$ are *known* coefficients associated with Dirichlet boundary conditions on part of $\partial\Gamma$, say $\partial\Gamma_D$, and $\{e_n\}$, $n = M+1, M+2, \dots, P$ are *unknown* coefficients associated with the bases on the part of the boundary $\partial\Gamma_N$ where the Neumann boundary conditions

$$\frac{\partial E_z}{\partial n} = f$$

are to be applied. Generalize the functional in order to include a boundary integral [similar to that appearing in Equation (3.5)] in the corresponding matrix equation representing the contribution from the Neumann condition.

- (d) Generalize the functional to include an electric current source $J_z(x, y)$ within the region Γ .

P3.4 By a procedure similar to that used in Prob. P3.2, show that the functional

$$F(\bar{A}) = \frac{1}{2} \iint_{\Gamma} \left(\frac{1}{\mu_r} \nabla \times \bar{A} \cdot \nabla \times \bar{A} + k^2 \epsilon_r \bar{A} \cdot \bar{A} \right) dx dy + \int_{\partial\Gamma} \frac{1}{\mu_r} \bar{A} \cdot \bar{h} dt$$

is stationary about the solution $\bar{A} = \bar{E}$, where \bar{E} satisfies the two-dimensional vector Helmholtz equation

$$\nabla \times \left(\frac{1}{\mu_r} \nabla \times \bar{E} \right) - k^2 \epsilon_r \bar{E} = 0$$

subject to either Dirichlet boundary conditions of the form

$$\hat{n} \times \bar{E} = \bar{g} \quad \text{on } \partial\Gamma$$

or Neumann boundary conditions of the form

$$\hat{n} \times (\nabla \times \bar{E}) = \bar{h} \quad \text{on } \partial\Gamma$$

where \bar{g} or \bar{h} is specified. In other words, seek a solution of the form

$$\bar{A} = \bar{E} + \epsilon \bar{\Phi}$$

where $\bar{\Phi}(x, y)$ satisfies $\hat{n} \times \bar{\Phi} = 0$ on the portion of $\partial\Gamma$ where Dirichlet conditions are imposed, and show that $F(\bar{A}) - F(\bar{E}) = O(\epsilon^2)$ as $\epsilon \rightarrow 0$.

P3.5 Using Maxwell's equations, show that the boundary condition $\hat{n} \times \bar{E} = 0$ is equivalent to

$$\frac{\partial H_z}{\partial n} = 0$$

for the TE polarization. In the general three-dimensional case, what would be an equivalent boundary condition applied to \bar{H} on a p.e.c. surface?

P3.6 Demonstrate that Equation (3.17) is equivalent to the Sommerfeld RBC in the limit as $a \rightarrow \infty$.

P3.7 Suppose that the imbedded p.e.c. boundary considered in Section 3.2 is replaced by a surface $\partial\Gamma_c$ over which, for the TM polarization, an impedance boundary condition

$$E_z = \eta_s H_t$$

holds. Describe the modifications necessary in order to incorporate the impedance boundary condition into the formulation described in Section 3.4.

P3.8 (a) Equation (3.25) is written with the "total" field as the primary unknown. However, the scalar Helmholtz equation can be manipulated into a slightly different "weak" equation, written for the TE case as

$$\begin{aligned} & \iint_{\Gamma} \left(\frac{1}{\epsilon_r} \nabla T \cdot \nabla H_z^s - k^2 T H_z^s \right) dx dy - \int_{\partial\Gamma} T \frac{\partial H_z^s}{\partial n} dt \\ &= \iint_{\Gamma} T \left[\nabla \cdot \left(\frac{1}{\epsilon_r} \nabla H_z^{\text{inc}} \right) + k^2 H_z^{\text{inc}} \right] dx dy \end{aligned}$$

in which the "scattered" field constitutes the primary unknown. Using the TE form of Equation (3.17) as a radiation boundary condition, develop the complete scattered field equation describing the H_z -field within an inhomogeneous cylinder.

(b) What are the essential differences between the total and scattered field formulations? Is the matrix operator different? Does the similarity of the matrix suggest any conclusion regarding the relative accuracy of either approach?

(c) Describe the implementation of boundary conditions on imbedded perfect electric conductors or impedance surfaces within the scattered field formulation. Are these conditions more or less convenient than with a total field formulation?

P3.9 The error associated with linear interpolation on triangles is known to behave as $O(\Delta^2)$ as $\Delta \rightarrow 0$, where Δ is the longest edge in the mesh. From the numerical data for E_z presented in Table 3.2, construct a graph of the error in the field at the center of the cylinder as a function of Δ . Assume that the error is of order $O(\Delta^q)$ as $\Delta \rightarrow 0$ and find the real-valued exponent q that best fits the data.

P3.10 Suppose the scattering cross section σ_{TM} is to be computed by integrating over equivalent volumetric polarization currents, as described in Section 1.11. Describe the manner in which the polarization currents would be obtained from the coefficients of E_z for the TM polarization. What additional pointer arrays are necessary to carry out the calculations? (*Hint:* Review the volume MFIE formulation described in Section 2.7.)

P3.11 Maxwell's equations dictate that

$$\frac{1}{\mu_r} \frac{\partial E_z}{\partial n} = j\omega\mu_0 J_z$$

at the surface $\partial\Gamma_c$ of a perfect conductor. Consequently, for testing functions T located on $\partial\Gamma_c$, the weak equation in (3.5) can be rewritten in the form

$$\int_{\partial\Gamma_c} T J_z dt = \frac{1}{j\omega\mu_0} \iint_{\Gamma} \left(\frac{1}{\mu_r} \nabla T \cdot \nabla E_z - k^2 \epsilon_r T E_z \right) dx dy$$

Consider the use of this equation as a way of computing J_z at the surface of a conducting region imbedded in the volume Γ after the E_z -field has been calculated by the solution of Equation (3.30). Assuming that J_z is a piecewise-linear function along the perimeter of the p.e.c. region, develop a procedure for obtaining the coefficients as a secondary calculation. Discuss the advantages and disadvantages of this approach compared with the direct calculation

$$J_z = \frac{1}{j\omega\mu_0\mu_r} \frac{\partial E_z}{\partial n}$$

P3.12 Derive Equation (3.48) by carrying out the inversion of (3.47).

P3.13 Using the scalar Helmholtz equation, derive Equation (3.80) from (3.78).

P3.14 The third-order Bayliss–Turkel RBC can be obtained from Equation (3.79). Express the third-order condition in the form

$$\frac{\partial E_z^s}{\partial \rho} = \dots$$

Consider the numerical implementation of this RBC within a finite-element discretization employing linear interpolation functions. Is there an obvious difficulty associated with its use?

P3.15 The Bayliss–Turkel type of local absorbing boundary condition is just one of numerous RBCs that have been developed. Engquist and Majda have derived boundary conditions based on pseudo-differential operator theory (B. Engquist and A. Majda, "Absorbing boundary conditions for the numerical simulation of waves," *Math. Comp.*, vol. 31, pp. 629–651, 1977). If applied to a circular boundary, their second-order condition has the

form

$$\frac{\partial E_z^s}{\partial \rho} = \gamma(\rho) E_z^s + \delta(\rho) \frac{\partial^2 E_z^s}{\partial \phi^2}$$

where

$$\begin{aligned}\gamma(\rho) &= \left(-jk - \frac{1}{2\rho} \right) \\ \delta(\rho) &= \left(\frac{-j}{2k\rho^2} + \frac{1}{2k^2\rho^3} \right)\end{aligned}$$

The error associated with this RBC can be studied for cylindrical harmonics following a procedure similar to that described in Equations (3.85) and (3.86), in order to obtain

$$\text{Error}(n, \rho) = \left| \frac{k H_n^{(2)\prime}(k\rho) - (\gamma - n^2\delta) H_n^{(2)}(k\rho)}{k H_n^{(2)\prime}(k\rho)} \right|$$

Compare the accuracy of this RBC to that of the second-order Bayliss–Turkel condition by computing the error associated with each RBC for several values of n and ρ . For a circular boundary, which appears to be more accurate?

- P3.16** Verify the boundary integral element matrices in (3.93) and (3.94).
- P3.17** Rewrite Equation (3.87) in order to produce a scattered field formulation, as described in Prob. P3.8.
- P3.18** In Prob. P1.22, the two-dimensional scattering cross section σ_{TM} was expressed as an integral over E_z and H_ϕ on a circular boundary. In general, the error associated with approximating H_ϕ on the boundary can be significant and thus usually prevents us from employing the approach of Prob. P1.22 with the outward-looking formulations of Chapter 3. However, there is a way in which this might be accomplished.

- (a) By combining the second-order Bayliss–Turkel RBC with the result of Prob. P1.22, show that

$$\begin{aligned}\sigma_{\text{TM}}(\phi) \cong \frac{k}{4} & \left| \int_{\phi'=0}^{2\pi} \left\{ \left[\frac{\alpha}{jk} - \cos(\phi - \phi') \right] E_z^s(\phi') + \frac{\beta}{jk} \frac{\partial^2 E_z^s}{\partial(\phi')^2} \right\} \right. \\ & \times e^{jka \cos(\phi - \phi')} a d\phi' \left. \right|^2\end{aligned}$$

Discuss the implementation of this expression, assuming that E_z is represented by linear interpolation functions.

- (b) Compare the resulting expression with that obtained from the eigenfunction expansion described in Equations (3.39)–(3.41) by applying it to individual harmonics $E_z^s = E_n e^{jn\phi}$ in order to quantitatively characterize the approximation error.

- P3.19** By a coordinate transformation, the second-order Bayliss–Turkel RBC from Equation (3.80) can be expressed directly in terms of the normal and tangential variables along a particular boundary. By transforming the cylindrical coordinate system (ρ, ϕ, z) into the right-handed system (n, t, z) local to some region along the boundary, where the polar angle from $\hat{\rho}$ to \hat{n} is θ , show that the RBC can be written as

$$\begin{aligned}\frac{\partial E_z^s}{\partial n} &= \frac{\alpha - k^2 \sin^2 \theta}{\cos \theta} E_z^s + \tan \theta \frac{\partial E_z^s}{\partial t} + 2 \sin \theta \frac{\partial^2 E_z^s}{\partial n \partial t} \\ &+ \frac{\beta \rho^2 \cos^2 \theta - \sin^2 \theta}{\cos \theta} \frac{\partial^2 E_z^s}{\partial t^2}\end{aligned}$$

Identify the two factors that complicate the direct implementation of this RBC. Can you suggest a way of replacing the mixed-derivative term with a reasonable approximation?

P3.20 Develop explicit expressions for the entries of the matrices \mathbf{L} , \mathbf{M} , and \mathbf{e}^{inc} in Equation (3.104), assuming piecewise-linear basis functions are used to represent K_z , piecewise-constant basis functions are used for J_z , and Dirac delta testing functions are located in the center of each cell edge around the boundary.

P3.21 The *addition theorem* for Hankel functions is given by

$$H_0^{(2)}(kR) = \begin{cases} \sum_{n=-\infty}^{\infty} H_n^{(2)}(k\rho') J_n(k\rho) e^{jn(\phi-\phi')} & \rho < \rho' \\ \sum_{n=-\infty}^{\infty} J_n(k\rho') H_n^{(2)}(k\rho) e^{jn(\phi-\phi')} & \rho > \rho' \end{cases}$$

where R is defined in Equation (3.103).

- (a) Use the addition theorem in combination with Equations (3.101), (3.114), and (3.115) to derive Equations (3.117) and (3.118).
- (b) Repeat your derivation for the TE case to obtain (3.123) and (3.124).

P3.22 Recast the TM inward-looking formulation described in Section 3.12 for the TE polarization.

P3.23 Extend the inward-looking formulation of Section 3.12 in order to use a surface integral equation such as (3.101) on a boundary of arbitrary shape.